



UNIVERSITY OF LEEDS

This is a repository copy of *A review of Hyperloop aerodynamics*.

White Rose Research Online URL for this paper:

<https://eprints.whiterose.ac.uk/209137/>

Version: Accepted Version

Article:

Lang, A.J., Connolly, D.P., de Boer, G. et al. (3 more authors) (2024) A review of Hyperloop aerodynamics. *Computers & Fluids*, 273. 106202. ISSN 0045-7930

<https://doi.org/10.1016/j.compfluid.2024.106202>

© 2024, Elsevier. This manuscript version is made available under the CC-BY-NC-ND 4.0 license <http://creativecommons.org/licenses/by-nc-nd/4.0/>.

Reuse

This article is distributed under the terms of the Creative Commons Attribution-NonCommercial-NoDerivs (CC BY-NC-ND) licence. This licence only allows you to download this work and share it with others as long as you credit the authors, but you can't change the article in any way or use it commercially. More information and the full terms of the licence here: <https://creativecommons.org/licenses/>

Takedown

If you consider content in White Rose Research Online to be in breach of UK law, please notify us by emailing eprints@whiterose.ac.uk including the URL of the record and the reason for the withdrawal request.



eprints@whiterose.ac.uk
<https://eprints.whiterose.ac.uk/>

A Review of Hyperloop Aerodynamics

Alex J. Lang^a, David P. Connolly^b, Gregory de Boer^c, Shahrokh Shahpar^d, Benjamin Hinchliffe, Carl A. Gilkeson^c

^a*EPSRC CDT in Fluid Dynamics, University of Leeds, LS2 9JT, UK*

^b*Institute for High Speed Rail and System Integration, University of Leeds, LS2 9JT, UK*

^c*School of Mechanical Engineering, University of Leeds, LS2 9JT, UK*

^d*Department of Aeronautics, Imperial College London, SW7 2AZ, UK*

Abstract

Evacuated tube transport, also known as Hyperloop, is a proposed mode of ground transport that uses depressurised tubes to transport passengers and cargo at high-speeds. The aerodynamic flow regime of a Hyperloop system combines the characteristics of low Reynolds number, high Mach number, and confined/choked flow. This makes it unique compared to more commonly studied aerodynamic problems, and as such it is not yet well understood. This review aims to evaluate the current state of Hyperloop aerodynamics research. First, the effects of low Reynolds number and compressibility in confined flows are explored. Next, 1D analysis is used to determine the theoretical flow characteristics of the Hyperloop. Analytical expressions are derived for the isentropic and Kantrowitz limits, which divide the state-space of the flow into choked and unchoked regimes. The use of Computational Fluid Dynamics to model the flow in the system is then discussed. This is by far the most active area of Hyperloop research, and results from the literature are evaluated and combined here to give further predictions for the expected flow states, which depend on the blockage ratio and Mach number. Finally, aerodynamic design considerations are explored, including the pod and tube geometry, boundary layer transition, ground proximity, ambient temperature, tube breaches and mitigating flow choking using bleed systems.

Keywords: Hyperloop Aerodynamics, Evacuated Tube Transport, Vacuum Train, High Speed Ground Transport, Computational Fluid Dynamics

Nomenclature

β	Blockage Ratio	p	Pressure
γ	Specific Heat Ratio	q	Heat Transfer Rate
λ	Molecular Mean Free Path	R	Specific Gas Constant
ρ	Density	T	Temperature
A	Pod-Tube Gap Area	U	Absolute Speed
A_b	Breach Area	u	Velocity
c	Speed of Sound	Kn	Knudsen Number
d	Molecular Diameter	Re	Reynolds Number
f	Friction Coefficient	CFD	Computational Fluid Dynamics
k_B	Boltzmann Constant	DES	Detached Eddy Simulation
l	Characteristic Length	EET	Evacuated Tube Transport
M	Mach Number	LES	Large Eddy Simulation
m	Mass	MoC	Method of Characteristics
		RANS	Reynolds-Averaged Navier-Stokes

1. Introduction

With the world becoming increasingly connected, the demand for long-distance, high-speed transport can only be expected to grow. At present, global transport already accounts for 37% of CO₂ emissions in end-use sectors [1]. This poses significant sustainability issues, particularly as the world attempts to achieve net zero emissions in an effort to avoid the most devastating effects of climate change [2]. Improving the efficiency of rapid transport is therefore a high-priority to allow sustainable travel in the future.

A next-generation mode of high-speed ground transportation, known as evacuated tube transport (ETT), has been proposed as a faster, cheaper and more sustainable alternative to high-speed rail and short-haul aviation. The theoretical ETT system consists of passenger-carrying ‘pods’ which are transported through a network of tubes, held at a partial vacuum. This low-pressure environment deliberately reduces the aerodynamic drag on the pods, which is known to account for upward of 75% of the total resistance encountered by a conventional high-speed train [3]. In theory, reducing the drag in this way should allow a typical evacuated tube vehicle to travel efficiently at transonic speeds, in excess of 1000 km/h [4].

It is proposed that the high-speed propulsion of the pods could be achieved with linear induction motors [5]. These are a variation of conventional electromagnetic induction motors that are ‘unwrapped’ to generate linear rather than rotary propulsion. The rotor would be a metal fin mounted to the pod, while the stator (which consists of banks of electromagnets) and all other propulsion components would be housed within the track. This minimises the weight and complexity of each individual pod. Once the pods have been initially accelerated, the low-drag environment should allow them to maintain cruising speed for many miles without the need for re-acceleration. This reduces the proportion of the track that would need to include propulsion components.

In order to reach high speeds while maintaining efficiency and passenger comfort, the pods would be suspended above the track. Some early proposals suggested the use of air bearings [5], which generate a thin layer of high pressure air between the pod and the ground to maintain levitation. Most subsequent studies, however, have proposed a magnetic levitation (maglev) system [6, 7], as this technology is already proven and implemented in current high-speed rail networks. Maglev systems would require a higher power input than air bearings, but offer significant practicality benefits as they operate with higher ground clearance and allow greater controllability [8]. A thorough review of maglev technology for both levitation and propulsion, along with the various maglev implementations in conventional rail systems is given by [9]. In the past decade, significant initial research has also been conducted on the design and implementation of maglev systems specifically for ETT [10, 11, 12, 13, 14, 15, 16].

Designing a practical evacuated tube transport system will require decades of research and innovation in a number of areas, including aerodynamics, propulsion, levitation, tube design, and vacuum systems. The aerodynamic design,

and in particular the minimisation of drag in the system, is likely to pose one of the most significant challenges in achieving the theoretical speed and efficiency benefits of ETT. Therefore, this is currently the most active area of research. This review evaluates the current state-of-the-art in ETT research, with a primary focus on the aerodynamic design, and identifies future directions for the development of the concept.

2. History and Development

The fundamental ideas behind evacuated tube transport have been developed for many years under various names. The earliest known research was conducted in the 18th century, with George Medhurst and William Murdoch designing pneumatic tube systems used to transport goods by generating a partial vacuum [17, 18]. The idea of creating propulsion from differential air pressure later formed the basis for the development of atmospheric railways, of which Isambard Kingdom Brunel was a strong proponent. These were seen for a short while as a viable alternative to traditional steam trains, but were ultimately abandoned due to operational difficulties [19].

The first discussion of what could be recognised as the modern ETT concept was given by rocket engineer Robert Goddard in the early 1900s [20], who postulated that a future ultra high-speed rail system would require trains to be magnetically levitated and travel through evacuated tubes. A few attempts were made to realise such a system in the following decades [21, 22], the most notable of which was the EPFL Swissmetro project [23] in the 1970/80s. This was proposed as a fully underground vacuum train that would link the major cities of Switzerland at speeds of up to 500 km/h. A small amount of aerodynamics research has been published on the concept, which includes the development of a 1D numerical code for simulation of the system [24]. This is discussed further in section 4.4. Swissmetro has never made it past the preliminary investigation stage, though there have been more recent attempts to revive the project [25, 26]. A similar project was undertaken by ET3 [27, 28] around the same time, again without commercial success thus far. Some initial academic studies were performed following these proposals, mostly involving aerodynamics simulations [29, 30, 31, 32, 33, 34].

The name *Hyperloop* was coined by Elon Musk and SpaceX in 2013 when they published ‘Hyperloop Alpha’ [5], a white paper outlining the ETT concept. The white paper provided a high-level discussion of many of the fundamental Hyperloop components, including the pod, tube, levitation and propulsion systems along with some initial design parameters. Following this, SpaceX ran an annual competition for university teams to design and test scaled Hyperloop pods on a purpose built low-pressure track. The analysis of the design of these pods formed some of the first published research on Hyperloop aerodynamics [35, 36, 37].

Since Musk’s contribution, the Hyperloop concept has developed significantly, with many academic studies and attempts at realising prototype models. A substantial body of literature surrounding ETT has been generated, with

research into various aspects of the system. This includes pod aerodynamics [35, 36, 38, 39, 40, 41], propulsion/levitation systems [7, 8, 10, 11] and energy consumption [42, 43], along with variations on the concept, such as the use of heliox gas in the tube to achieve the low-density benefits without the requirement of a near-vacuum [44]. In recent years, a number of private companies looking to commercialise a full scale Hyperloop system have begun developing facilities for testing pod and tube systems [4, 45, 46, 47, 48, 49, 50, 51], the details of which are summarised in [52]. The most notable of these is the Hyperloop One (formerly Virgin Hyperloop) [4] development system, consisting of a 500 m tube operating at a pressure of 100 Pa. This was used to conduct the first successful passenger tests in 2020 at 173 km/h with a 2-passenger pod.

3. Aerodynamic Flow Regime

The aerodynamics of a Hyperloop pod share a number of characteristics with (i) conventional trains, due to the geometric similarities and (ii) high-altitude aircraft, which operate with low external pressure, often in a transonic flow regime. Despite these apparent similarities, the aerodynamics of the ETT system will be in a separate class to any current vehicle type, due to the sealed tube environment and the expected low Reynolds number of the flow. The interaction of these two aspects, coupled with the transonic speeds, makes the aerodynamic design of an ETT system a formidable challenge.

3.1. Low Reynolds Number Aerodynamics

With an operating pressure of 100 Pa, as suggested by Musk [5] and Hyperloop One [4], the air density in a Hyperloop tube would be $1.2 \times 10^{-3} \text{ kg/m}^3$. These properties are reduced by a factor of 1000 in comparison to sea-level conditions, and are equivalent to the upper stratosphere at around 50 000 m [53]; this is significantly higher than the absolute ceiling of conventional aircraft. This reduced air density means that the flow around a pod will be at a low Reynolds number. Using the height of the pod (around 2 m [5]) as a characteristic dimension, the Reynolds number, Re , would be of the order 10^4 at transonic speeds. This is two orders of magnitude less than conventional trains or aircraft [3, 54]. Consequently, analysis of vehicle aerodynamics in this low Reynolds number regime has not received much attention and it is therefore not well understood. To illustrate this, the general Reynolds number and speed regimes for a range of moving objects are compared in figure 1, underlining the unique flow regime of ETT.

Differing conventions for the characteristic length mean that only very general comparisons of the Reynolds number can be made between different vehicle types. The convention for trains is to use the height (as the length varies with the number of carriages), while for aircraft the mean aerodynamic chord length of the wing is normally used. An argument could be made for adopting either of these conventions (height or length) for the Hyperloop concept. Taking

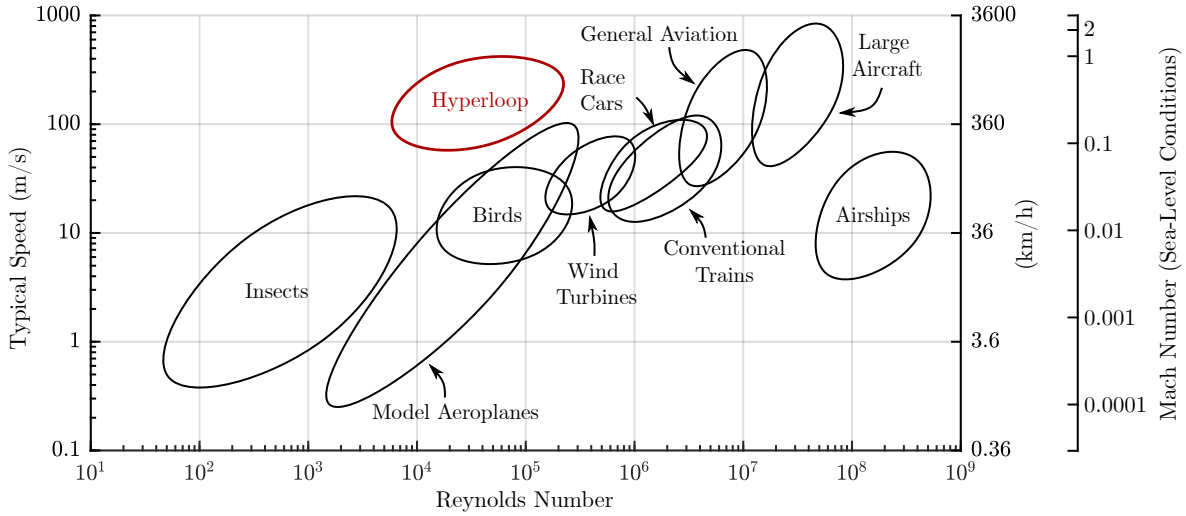


Figure 1: General operating speed and characteristic Reynolds number regimes for different moving objects. Adapted from [54] with additional data from [3, 5, 55].

the pod height is intuitive as the geometries are likely to be based on traditional train designs. On the other hand, the boundary layer and drag characteristics are important in studying the Hyperloop, and would be better parameterised by the length of the pod. Compared to the height based Reynolds number calculated above, the length based Re would be approximately 10 times higher, i.e. of the order 10^5 . Further arguments could also be made for using the tube diameter or the gap between the pod and the walls as the characteristic dimension.

It is also worth noting that the Reynolds numbers discussed are only small in the context of vehicle aerodynamics. In a more general fluid dynamics setting, ‘low Reynolds number’ is often used to describe viscosity dominated flows without significant inertial effects, as is the case for highly viscous fluids or small scale, slow moving flows. Swimming bacteria, for example, have $Re \approx 10^{-6}$ [56].

Although high Reynolds number aerodynamics covers the majority of conventional settings, a number of applications have been studied for which the flow is at a low Reynolds number. These applications include micro-air vehicles (MAVs) [57], small wind turbines [54, 58] and, more recently, the design of aircraft for use in the low-pressure atmosphere on Mars [59, 60].

The aerodynamics of a body at low Reynolds number can exhibit characteristics not observed in higher Re flows, particularly due to the strong influence of laminar boundary layer separation and transition to turbulence. These effects have been extensively studied through experimentation and measurements of the flow generated around aerofoils at low Reynolds numbers [54, 61, 62].

For high Re flows, the boundary layer formed on the surface of a body will generally transition from laminar to turbulent very quickly. At low Reynolds number, however, the boundary layer can remain laminar for a significant

distance. Turbulent boundary layers cause higher friction drag, but laminar boundary layers are far less tolerant to adverse pressure gradients. As such, laminar separation is commonly observed at lower Reynolds number [54]. Once the boundary layer has separated, growing instabilities trigger a transition to turbulence in the separated shear layer, which may then be able to reattach to the surface of the body. This flow phenomenon is known as a laminar separation bubble. Laminar separation bubbles are known to strongly influence aerodynamic characteristics by increasing drag and reducing lift [61]. This has implications in vehicle design and in most applications, including Hyperloop, reducing the length and height of separation bubbles will be beneficial (primarily by lowering the drag). This is particularly important for the design of aircraft, where the lift-drag ratio is critical to performance, especially in relation to range and endurance.

3.2. Blockage and Compressibility Effects

As already noted, the aerodynamics of the ETT system will be strongly influenced by the effect of the enclosed tube environment. In general, when a body moves through a fluid such as air, a high-pressure stagnation region is formed at the front (nose) and a low-pressure wake region at the rear (tail). If this motion is confined within a tube, the body behaves like a leaky piston in a cylinder, pushing air in front of, and around itself, while pulling the air behind. This principle is commonly referred to as the ‘piston effect’ in the context of trains travelling through tunnels [3], and is illustrated in figure 2. Mass conservation dictates that air is accelerated through the constriction between the body and the walls (ignoring compressibility for the moment). This results in a higher nose-to-tail pressure difference when compared to free-air motion. Thus, higher pressure drag is experienced by the body, as well as higher skin friction due to the local increase in the air speed and density [3]. The strength of the piston effect and the drag increase on the body is dependent on the blockage ratio, β , defined as the ratio between the projected frontal area of the body, A_{pod} , and the area of tube cross-section, A_{tube} . In general, higher blockage causes higher drag, so for the greatest aerodynamic efficiency, a Hyperloop should be designed to minimise the blockage ratio. The trade-off with this principle, however, is that larger tubes increase construction costs and vacuum requirements. There must also be a lower limit imposed on the pod size to maintain the comfort of passengers.

At higher speeds, compressibility effects play a more significant role in the aerodynamics, and flow choking becomes an issue. Choked flow describes a state in which the flow through the narrowest constriction in the system becomes sonic. An increase in speed when the flow is choked cannot increase the mass flow rate through the narrowest section, and so the mass of air continually builds up in front of the pod. This would be highly undesirable in ETT, as the cumulative build-up of air would cause the drag to increase with running time. The flow in a system with a lower blockage ratio will choke at a higher pod Mach number. Therefore, decreasing the blockage ratio would allow for greater top-speeds without the flow choking, though there are downsides of this which have been discussed above. A

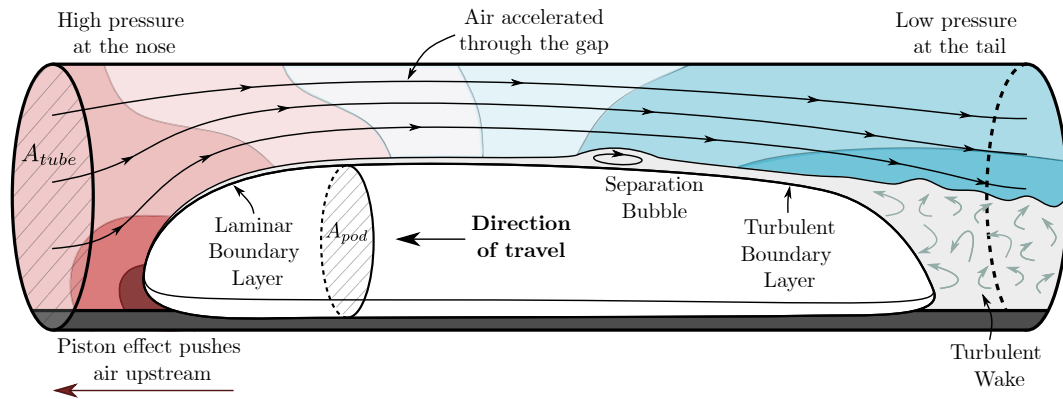


Figure 2: The piston effect and general expected pressure distribution generated by a Hyperloop pod travelling in a tube (in the absence of shocks). Streamlines indicate the flow from the pod frame of reference.

second mitigation strategy has also been proposed which involves a bleed system being incorporated into the pods to reduce the mass accumulation effects and alleviate the associated pressure build-up [5, 63].

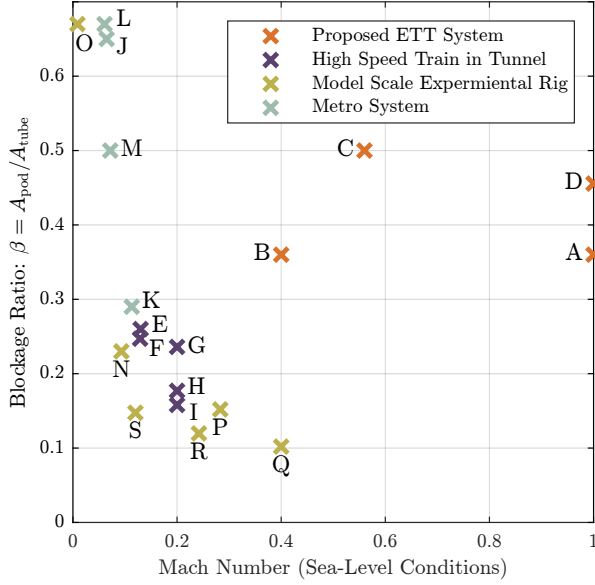
At the transonic speeds proposed for Hyperloop, the generation and propagation of shocks is also to be expected in the system [41]. This introduces an additional layer of complexity to the aerodynamics of the system, which must be carefully considered in the design process.

The blockage ratio and pod Mach number are the two most fundamental parameters in the design of an evacuated tube transport system. The influence of these two parameters is well understood in relation to conventional train-in-tunnel systems as a result of extensive theoretical, numerical, and experimental research [3, 64]. Typical blockage ratios and Mach numbers for conventional systems are compared with those proposed for ETT in figure 3.

Conventional high-speed trains rarely have a blockage ratio above 25% or Mach number above 0.2 when travelling through tunnels. This is partly due to the increase in drag caused by high speed and blockage, though mainly it is to limit the strength of the pressure waves generated within the tunnel. As a high-speed train transitions from free air to the enclosed environment, rapid pressure changes cause discomfort to the passengers, and the transient compression waves generated in the tunnel can form shock waves. This is known to cause ‘tunnel boom’ at the tunnel exit [65, 66].

Metro trains can have a much higher blockage ratio, up to around 70% for a single-track tunnel (the blockage is significantly lower for dual- or quad-track tunnels [67]). This high blockage ratio and the associated piston effect is advantageous as it is used to enhance the ventilation in underground systems [68]. Metro systems are not designed for high cruising speeds due to the frequent stopping of the trains, and as such the Mach number rarely exceeds 0.1.

Proposed ETT systems sit in a previously unexplored regime of high Mach number and relatively high blockage ratio. Therefore, the understanding of the aerodynamics in conventional systems can only go so far in predicting the flow characteristics in ETT.



Label	System	Location	Ref.
A	Hyperloop Alpha	USA	[5]
B	Swissmetro	Switzerland	[25]
C	Hardt Hyperloop	Netherlands	[47]
D	HyperloopTT	USA	[46]
E	Channel Tunnel	UK/France	[69]
F	Seikan Tunnel	Japan	[70]
G	Gotthard Base Tunnel	Switzerland	[71]
H	Katzenberg Tunnel	Germany	[72]
I	Terranuova Le Ville Tunnel	Italy	[73]
J	London Underground - Victoria Line	UK	[74]
K	Chongqing Rail Transit - Line 27	China	[75]
L	Toronto Subway - Line 1	Canada	[67]
M	Chicago 'L' - Milwaukee-Dearborn Line	USA	[67]
N	TRAIN Rig 1:25 Scale	UK	[76]
O	Model Subway 1:20 Scale	Republic of Korea	[77]
P	High-Speed Train Model 1:20 Scale	China	[78]
Q	High-Speed Train Model 1:8 Scale	China	[79]
R	Axisymmetric Train Model 1:97 Scale	Japan	[80]
S	Simplified Train Model 1:87 Scale	UK	[81]

Figure 3: Mach number and blockage ratio comparison for train in tube systems. The cross sectional area of a high-speed train was assumed to be 11 m^2 [82] where more specific data was not available.

4. Flow Modelling and Theoretical Analysis

Numerical and theoretical methods have been used to study and model the aerodynamics of the ETT system within the literature. Theoretical methods mainly involve quasi-1-dimensional analysis, using the equations of isentropic flow, along with shock relations. The vast majority of studies have been carried out numerically with Navier-Stokes based Computational Fluid Dynamics (CFD), using a mixture of commercial and in-house software. Only one recent experimental study of the aerodynamics in a model Hyperloop-type system has been published. This has led to difficulties in validating numerical and theoretical results. Most authors have therefore provided indirect validation of their methods, against related systems with similar expected flow features and parameters to Hyperloop.

4.1. Continuum Approximation

The modelling methods described in this section are based on the continuum approximation, which is the assumption that the fluid behaves as a continuous mass and that discrete particle effects can be neglected. This holds for the majority of aerodynamic flows, but may not be valid in cases involving rarefied gases. The Knudsen number, Kn , defined as the ratio of the molecular mean free path, λ , to the characteristic length scale of the flow, l , can be used to determine whether the approximation is valid [35, 83]:

$$Kn = \frac{\lambda}{l} = \frac{k_B T}{\sqrt{2} \pi d^2 l p}, \quad (4.1)$$

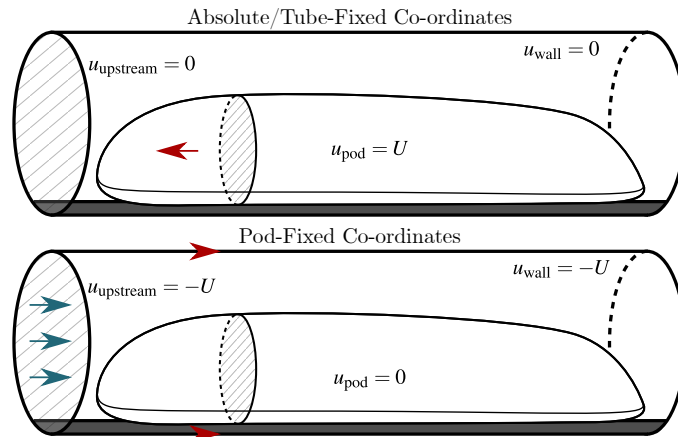


Figure 4: Comparison of the pod-fixed and tube-fixed (or absolute) co-ordinate systems. U is the absolute speed of the pod and u denotes a velocity in the relevant coordinate system.

where k_B , T , d and p are the Boltzmann constant, temperature, molecular diameter and pressure, respectively.

For a Hyperloop, the characteristic dimension (e.g. pod height) can be taken as $l = 2$ m, along with pressure $p = 100$ Pa, temperature $T = 300$ K and molecular diameter $d = 3.7 \times 10^{-10}$ m [83]. These values give a Knudsen number $Kn \sim 10^{-5}$. The mean free path is therefore far smaller than the characteristic length, and the Knudsen number is within the accepted limit $Kn < 10^{-2}$ for the continuum approximation to hold [84].

To check that is the case everywhere in the flow, the smallest length scale can also be considered. This is likely to be found in the suspension gap under the pod, which would typically be of the order 1 cm for a maglev system [8]. Using this length, the Knudsen number could be up to $Kn \sim 10^{-3}$ (though likely much lower as the pressure in this region will be significantly above the ambient value). The continuum approximation should therefore be valid everywhere in the flow.

4.2. Reference Frames

The expected flow field generated around a Hyperloop can generally be considered in two different frames of reference (or co-ordinate systems), depending on the characteristics of the flow being discussed. The simplest frame of reference is one in which the tube is stationary and the pod is moving, inducing a flow in the otherwise stationary air. This is often referred to as the *absolute*, *stationary*, or *tube-fixed* frame of reference. The latter notation is used here.

At times it may be more convenient to consider the system in a frame of reference where the pod is stationary and air is being blown past at the pod speed. In this case, the walls must also move at the pod speed to give the correct motion relative to the pod. This is known as the *pod-fixed* frame of reference, and is particularly useful when simulating steady ETT flows and presenting the results. To convert a flow field from the tube-fixed to the pod-fixed

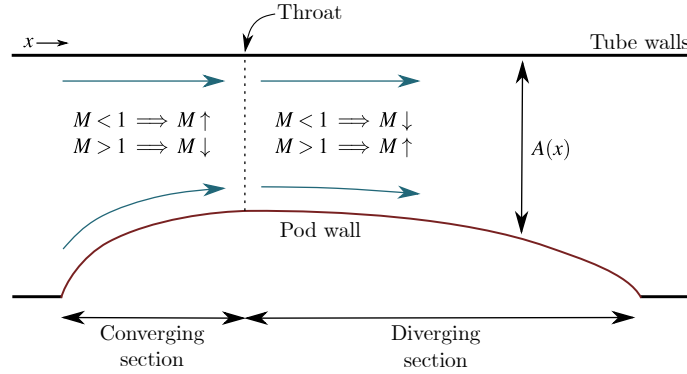


Figure 5: 1D approximation of an ETT system as a converging-diverging duct. $A(x)$ is the area of the gap between the pod and the tube, which parameterises the system. For subsonic upstream speeds (i.e pod speeds), the flow is accelerated in the converging section and decelerated in the diverging section. For supersonic speeds, the converse holds.

frame of reference, the pod speed is simply subtracted from the local velocity at each point.

A third frame of reference is sometimes considered, in which the shock wave upstream of the pod is stationary. This is known as the *shock-fixed* co-ordinate system [85].

4.3. 1D Isentropic Flow

In the simplest case, a Hyperloop can be approximated by a quasi-1-dimensional system. Here, the fluid domain is parameterised by its cross-sectional area, which is the area of the gap between the pod and the tube walls. This area, denoted by A , can be calculated as the difference between the cross-sectional area of the tube and of the pod at a given point. In the pod fixed frame of reference, this area is a function only of axial position in the tube, x , and so $A \equiv A(x)$. If the flow is steady and changes in A are gradual enough, other flow parameters such as speed, u , pressure, p , and density, ρ , can also be assumed to vary only with position along the tube. That is $u \equiv u(x)$, $p \equiv p(x)$, $\rho \equiv \rho(x)$ etc. For the quasi-1D assumption to hold, the flow must be uniform at any cross section, and so viscous effects such as boundary layers on the walls must be neglected. The fluid is therefore taken to be inviscid. If it is also assumed that the flow is adiabatic and no shock waves are generated, then the flow is *isentropic*, i.e., the entropy is constant in the system.

The Hyperloop system, viewed in pod-fixed co-ordinates, has therefore been reduced to the problem of isentropic flow through a fixed-geometry duct, with a cross section which converges and then diverges (as illustrated in figure 5). Convergent-divergent (C-D) ducts are widely used in engineering applications, and their flow characteristics are well understood. As such, some of the general flow features expected in a Hyperloop can be inferred from 1D duct analysis.

An important feature of a C-D duct is the area-velocity relationship [86], which can be expressed as

$$\frac{dA}{A} = (M^2 - 1) \frac{du}{u}, \quad (4.2)$$

where M is the local flow Mach number. The sign of the $(M^2 - 1)$ factor changes from negative for $M < 1$ (subsonic flow) to positive for $M > 1$ (supersonic). The implication of this is that for subsonic flow, an increasing (divergent) area gives a decrease in velocity, while for supersonic flow this gives a velocity increase. The converse is also implied for a decreasing (convergent) area. This is highlighted in the 1D Hyperloop approximation in figure 5.

The steady-state isentropic flow of an ideal gas through a duct can be further analysed using the following equations [84, 86]

$$p = \rho RT, \quad (4.3)$$

$$c = \sqrt{\gamma RT}, \quad (4.4)$$

$$M = u/c, \quad (4.5)$$

$$\frac{T_0}{T} = 1 + \frac{\gamma - 1}{2} M^2, \quad (4.6)$$

$$\frac{p_0}{p} = \left(\frac{\rho_0}{\rho}\right)^\gamma = \left(\frac{T_0}{T}\right)^{\frac{\gamma}{\gamma-1}}, \quad (4.7)$$

where R is the specific gas constant, T is the local temperature, c is the local speed of sound and γ is the specific heat ratio. The subscript 0 denotes a total quantity (e.g. total temperature T_0). Using the above equations, the mass flow rate, \dot{m} , through any cross section can be expressed as

$$\dot{m} = \rho u A = M A p_0 \sqrt{\frac{\gamma}{RT_0}} \left(1 + \frac{\gamma - 1}{2} M^2\right)^{-\frac{\gamma+1}{2(\gamma-1)}}. \quad (4.8)$$

4.3.1. Choked Flow and the Isentropic Limit

The most critical characteristic of duct flows that is relevant for evacuated tube transport is the concept of flow choking. Choked flow is the condition in which the flow through the narrowest constriction in the system, referred to as the *throat*, is sonic ($M = 1$). A conventional C-D duct (e.g. in a wind tunnel) is driven by an upstream-downstream pressure difference, and in this case, choked flow represents a limiting case whereby any further decrease in downstream pressure will not increase the mass flow rate through the system.

The equation for the choked isentropic flow in a C-D duct can be calculated from equations 4.3-4.7 as follows. Under the assumption of steady flow, the mass flux, \dot{m} , through any cross section must be constant due to conservation.

Equating the mass flow rate (given by equation 4.8) through the throat with another general cross section gives

$$\begin{aligned} \dot{m} &= MAp_0 \sqrt{\frac{\gamma}{RT_0}} \left(1 + \frac{\gamma-1}{2} M^2\right)^{-\frac{\gamma+1}{2(\gamma-1)}} \\ &= M^* A^* p_0^* \sqrt{\frac{\gamma}{RT_0^*}} \left(1 + \frac{\gamma-1}{2} M^{*2}\right)^{-\frac{\gamma+1}{2(\gamma-1)}}, \end{aligned} \quad (4.9)$$

where * denotes quantities at the throat. Choked flow implies that $M^* = 1$, and the isentropic assumption means that total quantities (p_0, T_0) are constant. With this, the relationship can be written as

$$\frac{A^*}{A} = M \left(1 + \frac{\gamma-1}{2} M^2\right)^{-\frac{\gamma+1}{2(\gamma-1)}} \left(\frac{\gamma+1}{2}\right)^{\frac{\gamma+1}{2(\gamma-1)}}. \quad (4.10)$$

This is commonly referred to as the *area-Mach number relation* [86]. In a pressure-driven system with choked isentropic flow, this gives the Mach number at any point as a function only of the local area and throat area.

The fundamental difference between the Hyperloop and a C-D duct in, for example, a wind tunnel is that the system is not driven by pressure differences, but rather by the pod velocity. In pod-fixed coordinates, this means that the upstream flow Mach number is determined by the pod speed, M_{pod} . Applying the area-Mach number relation far upstream therefore gives the specific pod Mach number at which the flow will choke for a given throat-to-tube area ratio. This is often referred to as the *critical Mach number* [38]. The convention for Hyperloop and trains in tunnels is to express this in terms of the blockage ratio, β :

$$\begin{aligned} \beta &= \frac{A_{\text{pod}}}{A_{\text{tube}}} = 1 - \frac{A^*}{A_{\text{tube}}} \\ &= 1 - M_{\text{pod}} \left(1 + \frac{\gamma-1}{2} M_{\text{pod}}^2\right)^{-\frac{\gamma+1}{2(\gamma-1)}} \left(\frac{\gamma+1}{2}\right)^{\frac{\gamma+1}{2(\gamma-1)}}, \end{aligned} \quad (4.11)$$

where it is assumed that the frontal area of the pod, A_{pod} , is equivalent to the maximum cross-sectional area of the pod, i.e. at the throat. This is likely to be the case in general. In the context of ETT, this equation is known as the *isentropic limit* [87]. For a given blockage ratio, if the pod Mach number is below this limit then the flow does not choke and remains steady, subsonic and isentropic everywhere. If the Mach number is above this isentropic limit, however, the flow is choked and the mass flow rate through the throat is limited. This causes mass to be continually accumulated upstream of the pod. In this choked regime the flow can no longer be isentropic, and a normal shock is generated upstream which separates away from the pod with time [85, 39].

4.3.2. Shocks, Unchoking and the Kantrowitz Limit

Both normal and oblique shocks will be generated in the ETT system, even with pod speeds that are well below sonic [85]. Entropy is increased across a shock, therefore the isentropic relations given in the previous section cannot be applied directly when shocks are present. In order to circumvent this, a shock is assumed to be an infinitely thin discontinuity across which the flow parameters change, and the flow upstream and downstream of a shock is taken as isentropic. Shocks do not break the adiabatic assumption and so total temperature will be conserved, whereas total pressure will decrease across the shock. For a normal shock, the ratio of the total pressures can be expressed in terms of only the upstream Mach number [88]:

$$\frac{p_{0,u}}{p_{0,d}} = \left[\frac{(\gamma + 1)M_u^2}{(\gamma - 1)M_u^2 + 2} \right]^{-\frac{\gamma}{\gamma-1}} \left[\frac{\gamma + 1}{2\gamma M_u^2 - (\gamma - 1)} \right]^{-\frac{1}{\gamma-1}}, \quad (4.12)$$

where subscripts u and d denote conditions upstream and downstream of the shock respectively.

For pod velocities in the choked flow range, a normal shock is expected to be generated upstream in the tube. In this way, the Hyperloop acts in a similar fashion to a supersonic aircraft intake [89]. Supersonic intakes are converging-diverging diffusers, used to take in air and reduce it from the free-stream speed. To function correctly, these supersonic diffusers must be ‘started’, a process which involves a normal shock passing through the throat (the shock is said to be ‘swallowed’). If the throat is too narrow, the flow will choke and the normal shock will sit off the front of the diffuser. This flow state is known as ‘unstart’, and directly corresponds to the choked supersonic Hyperloop case.

A simple relationship for determining the limiting blockage ratio and Mach number for which the flow will start in a supersonic diffuser was given by Kantrowitz and Donaldson [90]. This is derived by assuming that a stationary normal shock sits at the start of the converging section of the diffuser, with the flow choked at the throat. If the flow is taken to be steady, then it can be assumed isentropic either side of the shock. In the 1D ETT case, the tube area upstream of the shock is constant with $A = A_{\text{tube}}$ and thus the upstream flow has a constant Mach number ($M = M_{\text{pod}}$). The constant tube area also implies that the position of the shock could anywhere upstream without loss of generality. As the flow is assumed steady, the mass flow rate given in equation 4.9 can be equated between the upstream region and the throat (denoted by *) which is downstream of the shock, giving

$$\begin{aligned} \beta &= 1 - \frac{A^*}{A_{\text{tube}}} \\ &= 1 - M_{\text{pod}} \frac{p_{0,u}}{p_0^*} \left(1 + \frac{\gamma - 1}{2} M_{\text{pod}}^2 \right)^{-\frac{\gamma+1}{2(\gamma-1)}} \left(\frac{\gamma + 1}{2} \right)^{\frac{\gamma+1}{2(\gamma-1)}}. \end{aligned} \quad (4.13)$$

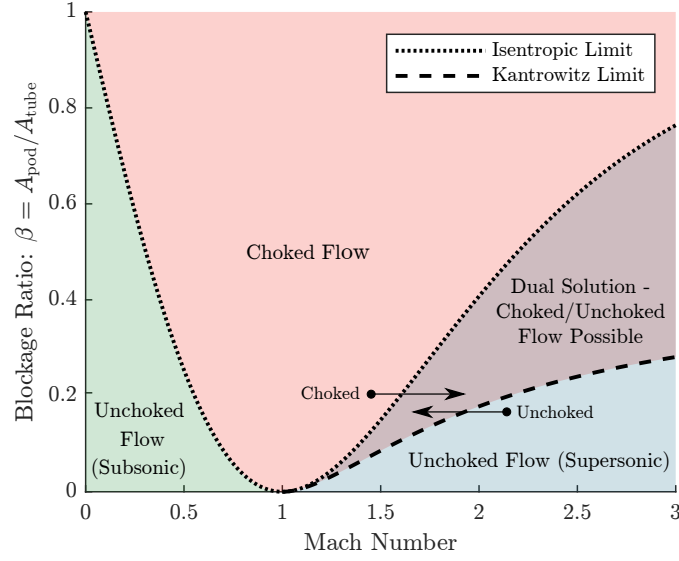


Figure 6: The expected flow choking behaviour of the Hyperloop, based on the isentropic limit (equation 4.11) and Kantrowitz limit (equation 4.15). To calculate the limits, the specific heat ratio was taken as $\gamma = 1.4$.

Again, the equation is written in terms of the blockage ratio, and the constant factors (including total temperature) have been cancelled out. This equation differs from the isentropic limit equation (4.11) only by a single factor due to the total pressure loss across the shock. Substituting the pressure ratio given in equation 4.12 gives

$$\beta = 1 - M_{\text{pod}} \left[\frac{(\gamma + 1)M_{\text{pod}}^2}{(\gamma - 1)M_{\text{pod}}^2 + 2} \right]^{-\frac{\gamma}{\gamma-1}} \left[\frac{\gamma + 1}{2\gamma M_{\text{pod}}^2 - (\gamma - 1)} \right]^{-\frac{1}{\gamma-1}} \left[1 + \frac{\gamma - 1}{2} M_{\text{pod}}^2 \right]^{-\frac{\gamma+1}{2(\gamma-1)}} \left[\frac{\gamma + 1}{2} \right]^{\frac{\gamma+1}{2(\gamma-1)}}. \quad (4.14)$$

After simplification, this can be written in the form [91]:

$$\beta = 1 - \left[\frac{(\gamma + 1)M_{\text{pod}}^2}{(\gamma - 1)M_{\text{pod}}^2 + 2} \right]^{-\frac{1}{2}} \left[\frac{(\gamma + 1)M_{\text{pod}}^2}{2\gamma M_{\text{pod}}^2 - (\gamma - 1)} \right]^{-\frac{1}{\gamma-1}}. \quad (4.15)$$

This equation is known as the *Kantrowitz limit* [92]. For a given blockage ratio, if the Mach number is higher than the Kantrowitz limit, the flow will be started and become unchoked. The mass flow rate through the throat can increase above the choked value in this regime and no normal shock is generated upstream. In the ETT case, a steady oblique or bow shock will sit at the nose of the pod.

The isentropic and Kantrowitz limits divide the flow state-space into choked and unchoked regimes, based on the blockage ratio and pod Mach number. The limits are plotted in figure 6, with the corresponding flow states highlighted. In the ETT literature, these limits are often confused, with the Kantrowitz limit erroneously being used to

describe the general point at which the flow chokes. The two limits are very much distinct and *both* are needed to fully characterise the flow state-space. A dual solution regime also exists for pod speeds between the supersonic isentropic and Kantrowitz limits, in which the flow may be choked or unchoked [93]. This is best explained by considering how the flow changes with acceleration and deceleration of the pod.

In normal operation the system is expected to undergo the following state changes. Initially, the pod will be accelerated from rest through the subsonic unchoked region. It will then accelerate past the subsonic isentropic limit which will cause the flow to choke and a normal shock to form upstream with its separation from the pod increasing over time. If the pod is further accelerated past the Kantrowitz limit, the separation between the normal shock and the pod will decrease with time until the pod reaches the shock. The flow will then unchoke and a stationary bow shock or oblique shock will sit at the nose.

When decelerating from speeds above the Kantrowitz limit, the flow will remain unchoked until the supersonic isentropic limit is reached. Below this speed, the flow will choke again and the departing normal shock is formed upstream again. Once the speed drops below the subsonic isentropic limit, the upstream shock should begin to dissipate. The flow therefore shows hysteresis in the dual solution regime, with the flow staying choked if accelerating into this regime from lower speeds and remaining unchoked if decelerating from higher speeds.

The asymptotic behaviour of the isentropic limit and Kantrowitz limit for large Mach numbers can also be determined from equations 4.11 and 4.15:

$$\lim_{M \rightarrow \infty} [\beta_{\text{Isentropic}}] = 1, \quad (4.16)$$

$$\begin{aligned} \lim_{M \rightarrow \infty} [\beta_{\text{Kantrowitz}}] &= 1 - \left(\frac{\gamma + 1}{\gamma - 1}\right)^{-\frac{1}{2}} \left(\frac{\gamma + 1}{2\gamma}\right)^{-\frac{1}{\gamma-1}} \\ &\approx 0.3998 \text{ (for } \gamma = 1.4\text{)}. \end{aligned} \quad (4.17)$$

The isentropic equation converges to a value of 1, which implies that for any Mach number, there will be a blockage ratio (<1) that would permit flow above the isentropic limit. Conversely, the Kantrowitz limit equation converges asymptotically to a fixed value <1 (≈ 0.4 for air under standard conditions). This means that any system with a blockage ratio greater than this asymptotic value can never permit flow above the Kantrowitz limit. Supersonic unchoked flow is therefore impossible for higher blockage ratios unless unchoking is achieved by some means other than simply accelerating to higher speeds (e.g. having a section of tube with greater area to initialise unchoked flow before reducing to the final area).

Operation in a choked flow state is likely to be unfeasible for Hyperloop, as the drag would continually rise due to mass accumulation ahead of the pod. This imposes restrictions on the feasible operating speeds of the Hyperloop. For

Blockage Ratio, β	Feasible Subsonic Range < Isentropic Limit		Feasible Supersonic Range > Kantrowitz Limit (Isentropic Limit)	
	Mach No.	Velocity (km/h)	Mach No.	Velocity (km/h)
0.1	$M < 0.68$	$u < 840$	$M > 1.58$ (1.39)	$u > 1950$ (1720)
0.2	$M < 0.55$	$u < 680$	$M > 2.19$ (1.60)	$u > 2700$ (1980)
0.3	$M < 0.46$	$u < 570$	$M > 3.33$ (1.79)	$u > 4070$ (2210)
0.4	$M < 0.38$	$u < 470$	$M > \text{N/A}$ (1.99)	$u > \text{N/A}$ (2460)

Table 1: Feasible pod speeds for unchoked flow with different blockage ratios. In the supersonic regime, the value in brackets is the isentropic limit value, above which the flow may be choked or unchoked. Above the Kantrowitz limit value, the flow must be unchoked. For $\beta = 0.4$ and above, flow above the Kantrowitz limit is not possible.

example, assuming a blockage ratio of 36% as suggested by Musk [5], then from figure 6 and equations 4.11, 4.15, the allowable flow speeds to guarantee unchoked flow are $M < 0.4$ ($u < 500$ km/h) or $M > 5.5$ ($u > 6800$ km/h). The Shanghai Transrapid Maglev already operates in the 400-500 km/h range [94], and so a Hyperloop with this blockage ratio operating below the choked flow speeds would offer little speed benefit. At the other end of the spectrum, travelling in the unchoked supersonic range (above the Kantrowitz limit) is also unfeasible as the track geometry would be restricted to curves with extremely large radii to limit the lateral forces experienced by passengers.

Table 1 explores further blockage ratios and identifies the feasible upper and lower speed ranges for unchoked flow. These examples suggest that very low blockage ratios would be needed if the flow is to be unchoked at realistic Mach numbers. Clearly this is impractical, as it would require either very small pods or large tubes. The 1D theory therefore highlights the need for an alternative method to mitigate flow choking without increasing the blockage ratio if the Hyperloop concept is going to be viable. This idea is considered further with a discussion of pressure bleed systems in section 6.9. It is also important to appreciate that the isentropic/Kantrowitz limits are based on 1D theory, which is a significant simplification of the full physics of the system.

4.3.3. Limitations and Extensions of Steady 1D Theory

The benefit of 1D methods is that they permit theoretical analysis for fundamental flow features and rapid solution times when used in numerical codes. However, there are limitations with this type of analysis. The most obvious limitation of 1D results is that by their nature, they can only reproduce spatially averaged flows and cannot resolve 2D/3D features such as oblique shocks.

The 1D theory also assumes that the flow is isentropic and no shocks are present below the isentropic limit. However, shocks may be generated at lower pod Mach numbers by a wave-steepening process. This occurs when the compression waves created by the motion of the pod in the tube become steeper and coalesce into a normal shock that travels upstream. This type of shock is well studied in the context of conventional trains in tunnels, and further detail of the mechanism by which these waves are generated is given in [95, 66]. Due to the Mach number being reduced

across the upstream normal shock, slightly higher pod Mach numbers may be attained before the flow becomes sonic at the throat and chokes. That is, the observed critical Mach number can be higher than the 1D isentropic limit as a result of the leading shock [85].

A further significant limitation of 1D isentropic theory is that the effects of viscosity and boundary layers are neglected. The boundary layer that grows on the pod will increase the *effective* blockage ratio, which acts to lower the critical Mach number, causing the flow to choke earlier. The impact of this behaviour becomes less significant as the speed increases due to the boundary layers becoming thinner. The relative magnitude of viscosity effects compared to the leading shock prediction issue is discussed further in section 5.3 with comparisons of the 1D theoretical limits to simulated results using higher-dimensional viscous methods.

Steady 1D theory can however be extended to capture the effects of some of the transient and non-isentropic physics of the system. For example, a simple method considering the flow in shock-fixed coordinates allows prediction of the propagation velocity for the transient normal shock generated in choked flow, together with flow quantities including pressure and density throughout the domain [85, 96]. Hou et al. [91] also derive limiting blockage ratios and Mach numbers at which a normal shock will detach from the tail of the pod in 1D, though this does not generalise to higher dimensions. Even further sophisticated analysis of the system is also possible by considering the time-dependent flow using numerical simulation.

4.4. Unsteady 1D Simulation

The steady 1D analysis presented so far gives a powerful method for predicting the state changes of the flow in an ETT system, as a function of the blockage ratio. This analysis can be extended further to model the transient aerodynamics of the system with corrections accounting for additional physics such as viscous drag and heat transfer. Unsteady 1D analysis has proven to be highly successful in the study of conventional trains in tunnels and there is a large body of research detailing the theoretical basis of such methods [97, 98, 3]. This is also supported by validation against model-scale experiments and full-scale field measurements [80, 24, 74, 99]. Notable 1D train-in-tunnel codes include ThermoTun [100] and NUMSTA [24], with the latter having been developed for the design of the proposed Swissmetro ETT system [23].

The starting point for such methods is typically the 1D, unsteady, compressible Euler equations along with the ideal gas equation of state (equation 4.3). Additional source terms can also be included to account for wall friction

and heat transfer using semi-empirical models. The general equations take the form [91, 101]:

$$\frac{\partial}{\partial t}(\rho A) + \frac{\partial}{\partial x}(\rho u A) = 0, \quad (4.18)$$

$$\frac{\partial}{\partial t}(\rho u A) + \frac{\partial}{\partial x}(\rho u^2 A + p A) - p \frac{\partial A}{\partial x} = F, \quad (4.19)$$

$$\frac{\partial}{\partial t}(\rho A E) + \frac{\partial}{\partial x}(\rho u A E + p u A) + p \frac{\partial A}{\partial t} = Q, \quad (4.20)$$

where

$$E = \frac{1}{\gamma - 1} \frac{p}{\rho} + \frac{u^2}{2}. \quad (4.21)$$

F here is a term accounting for skin friction at the tube and train walls and Q is a term that describes the rate of heat transfer. A variety of formulations for these terms exist in the literature, and details on how these are typically constructed for train-in-tunnel simulations can be found in [91, 80, 24, 102]. Additional loss coefficients based on the train geometry can also be introduced in correction terms to account for the locally 3D flow regions at the nose and tail [103]. The fundamental theory and derivation behind the 1D Euler equations can be found in classical textbooks such as [101].

The 1D Euler equations are hyperbolic, and can thus be solved via the method of characteristics (MoC) [101, 104]. To do this, the system is reduced to set of ordinary differential equations along a set of characteristic curves, which can then be integrated using iterative numerical methods [101]. MoC has typically been the most common choice of solution method in 1D train-in-tunnel codes (e.g. [100, 98, 80]). In more recent 1D codes however, the finite volume method has become more popular [91, 24, 103, 81]. This is a more general method in which the integral form of the Euler equations are evaluated on discrete control volumes, as described by Jameson et al. [105]. The finite volume method avoids some of the known limitations of MoC for higher Mach number flows where choking occurs [103, 106]. Traditional MoC codes were limited to low Mach numbers, which was sufficient for conventional train-in-tunnel simulations, but not for transonic ETT systems where flow choking may take place. More recently however, extensions to MoC codes have been shown to be accurate up to Mach 1 with choked flow [106, 104]. Finite volume methods such as those of Hou et al. [91] have been used to simulate ETT flows up to Mach 3. The finite volume code NUMSTA [24] and MoC code ThermoTun [100] have been found to give very similar results up to Mach 0.8 [106], which along with their respective experimental validation gives confidence in both numerical methods for modelling ETT flows.

The choice of boundary conditions used for modelling the system is of critical importance. Sophisticated boundary conditions that model open and closed tunnel ends, branches, cross passages and ventilation shafts have been

developed for 1D train-in-tunnel simulations [24, 80, 100].

4.5. Computational Fluid Dynamics

The majority of studies on Hyperloop aerodynamics have utilised Navier-Stokes based Computational Fluid Dynamics via general purpose commercial codes. These CFD simulations allow for relatively cheap and flexible analysis of the aerodynamics of the system in comparison to experiments, though require significantly more time than the 1D methods discussed previously. CFD allows for rapid testing with large sets of design parameters and a huge amount of measurable output data (e.g. lift and drag coefficients, surface pressure, heat transfer, shock strength and position).

4.5.1. Turbulence Modelling

The choice of turbulence model plays a crucial role in ensuring the accuracy of a CFD simulation. RANS models, and in particular the SST $k-\omega$ variant [107], are currently the most widely used in aerospace applications including Hyperloop research. However, conventional RANS methods have well-known limitations in modelling laminar-turbulent transition, particularly at low Reynolds numbers [108]. For high Reynolds number aerodynamics, any boundary layer forming on a surface will generally become turbulent very quickly, and the effect of this abrupt transition can be accurately captured by conventional RANS models. At lower Reynolds numbers, however, laminar boundary layers can persist for a significant distance before transition [109]. Conventional RANS models do not adequately capture this behaviour and can therefore give inaccurate lift/drag results, particularly when the body being simulated has strong curvature and a separation bubble is generated [110, 111]. Further detail on the historical development of turbulence modelling with consideration of transition and the associated limitations of popular models is given by Pope [112] and Wilcox [113].

The shortcomings of conventional RANS for low Reynolds number flows have, to some extent, been addressed with the introduction of transition RANS models, such as the $\gamma - \text{Re}_\theta$ [109, 114] and $k - k_l - \omega$ [115] models. These methods build upon the conventional models by incorporating additional transport equations to capture the transition to turbulence in the boundary layer. These methods are fully compatible with general-purpose CFD codes and give much improved accuracy for low Reynolds number flows where boundary layer transition is significant [109]. Another popular method for modelling transition is the e^N model [116, 117], which is based on linear stability theory. This method has proven to be highly successful when implemented in two dimensional viscous/inviscid codes such as XFOIL [118]. However, it has never been extended to general 3D Navier-Stokes CFD codes due to difficulties obtaining sufficient accuracy for the stability equations and tracking the growth of disturbances when using grids that are not aligned with the streamline direction [119].

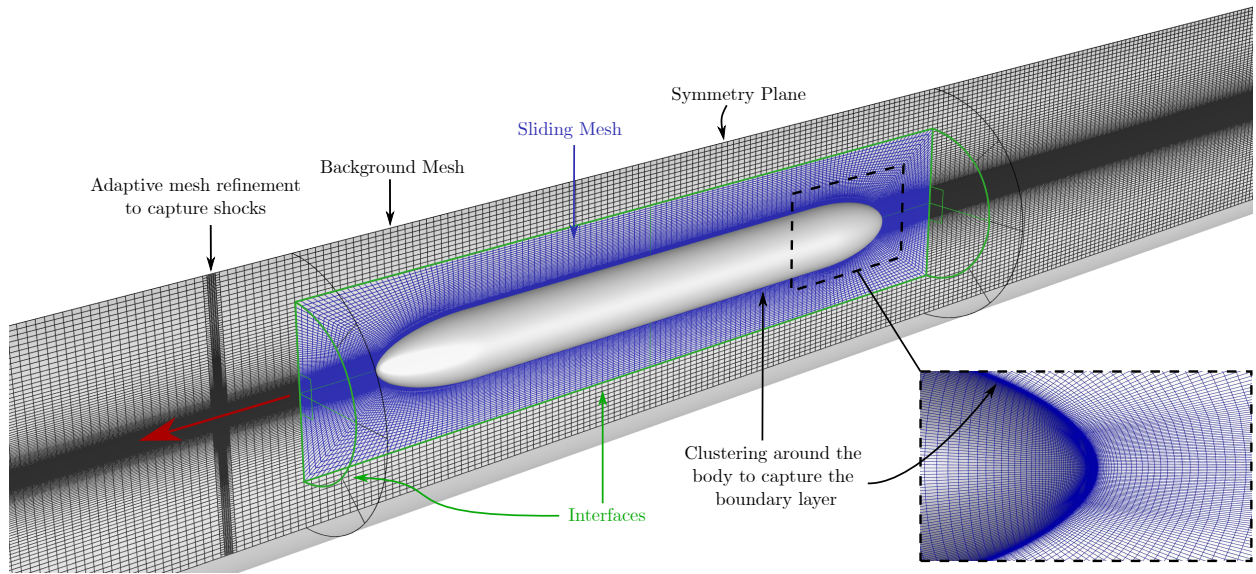


Figure 7: Typical sliding/overset CFD mesh set-up for a 3D CFD simulation of an ETT system with a symmetry plane (from present research).

The need for transition models in simulating a Hyperloop is debated. The Reynolds number of the flow places it within a regime in which boundary layer transition will have some effect, though laminar separation is unlikely as the pod is not inclined relative to the flow. A number of Hyperloop studies have used transition models [36, 37, 38, 120], though only a few have included any analysis of the transition effect (this is discussed further in section 6.6). As of yet, no study has quantified the impact of using transition models in comparison to conventional ones. It is therefore unclear whether transition models are necessary and worth the additional computational expense when simulating Hyperloop aerodynamics.

Scale-resolving methods, which directly resolve some portion the turbulent spectrum in the domain, can also capture transition and have been used to model the flow in Hyperloop systems. These high-fidelity methods include large eddy simulation (LES) and detached eddy simulation (DES), which combines LES with a RANS method to model the small-scale turbulence in wall boundary layers [121]. A number of authors have used DES to perform high-resolution analysis of the unsteady flow features. This includes the wake flow and shock patterns behind the pod [122], along with the effect of nose length [123, 124], Mach number [125] and the influence of the track [126]. However, LES and DES are prohibitively expensive for large parametric studies, and so tend to be reserved for detailed analysis of a small set of designs or parameters rather than iterative design optimisation studies.

4.5.2. Meshing

Advanced meshing techniques have been utilised in Hyperloop aerodynamics research. The most simple set-up uses a pod-fixed frame of reference with a static mesh. This method is the least expensive and allows for steady-state

simulation of the system. Many studies, however, use dynamic methods, with the Hyperloop system lending itself well to sliding overset meshes [125]. In this case, a simple structured background mesh can be generated for the tube, while a near-field mesh is created around the pod. The tube mesh stays fixed while the pod mesh is overset and slides through the domain at the pod speed, as shown in figure 7. The flow variables and fluxes are interpolated and transferred between the two meshes as the simulation progresses. This is a more complex meshing and solution process, though it is the most accurate way to model the flow physics.

The limitation with the sliding mesh method comes from the size of the tube mesh. Due to the high speed of the pod, the tube must be extremely long to simulate even very short time periods. For example, Niu et al. [124] required a >5 km tube to generate a 6 s simulation with a maximum pod speed of 555 m/s. Typical Hyperloop CFD simulations require mesh sizes of the order ~ 1 -10 million cells [38, 127, 125], though up to ~ 80 million have been used for high-fidelity, sliding mesh simulations [122].

Targeted clustering of the cells is required in order to capture the strong gradients in the flow, particularly in the boundary layer and the wake region [122, 123]. High mesh density is also required to accurately resolve any shocks, but the location of these shocks is not known a priori and they may not be stationary. Adaptive mesh refinement based on gradients in the solution is therefore used to modify the mesh in the region of the shocks as the simulation progresses.

4.5.3. *Boundary Conditions*

Typically, the no-slip condition is applied on the pod and tube walls [35]. If the simulation is performed in the pod-fixed frame of reference, the speed of the air must be set at the upstream end of the domain and the tube walls must be moving at the same speed [37]. As the flow is compressible, the upstream and downstream ends of the domain tend to be set as far-field pressure/characteristic conditions with the required Mach number (which is 0 in the tube-fixed frame of reference) [128, 129]. The symmetry of the system can also be leveraged to reduce the domain size, and thus mesh size, by applying symmetry plane conditions. Left-right symmetry can be assumed with little loss of generality, reducing the 3D domain size by half. Upper-lower symmetry is also used in some 3D simulations, giving another factor of 2 reduction. A full axisymmetry assumption can reduce the problem to 2D with a central axis, drastically reducing the computational expense, though this limits the pod design to very simple geometries and requires the pod to be radially centered in the tube. Alternatively, planar 2D simulations can be used to model a non-centered pod and ground proximity effects. This is equivalent to an assumption of a pod and tube with infinite span, which is an unrealistic representation of the physics of the system and gives rise to inaccurate blockage effects.

Authors	Case/Geometry	Reynolds Number (Million)	Mach Number	Effective Blockage Ratio	Examples of Usage
Stine et al. [131]	Hemispherical Nose	0.60 - 4.0	2.0 - 3.8	3%	[63, 92, 127, 132, 133]
Guerra et al. [134, 135]	Scramjet Combustion Chamber	0.15	2.0	3%	[128, 133, 136]
Li et al. [137]	Hypersonic Intake Isolator	8.7 - 17	1.9 - 4.9	7%	[122, 123, 138]
Reinartz et al. [139, 140]	Hypersonic Intake Isolator	48 - 51	2.4 - 3.0	N/A	[127, 141]
Saito et al. [80]	Model Train in Tube	0.18 - 0.30	0.24 - 0.40	12%	[123, 142]
Waidmann et al. [135]	Scramjet Combustion Chamber	0.15	2.0	3%	[128, 133]
Gao et al. [144, 143]	Scramjet Combustion Chamber	3.7	3.0	N/A	[122]
Kayser and Whiton [145]	Boattailed Projectile	1.1 - 1.5	0.91 - 1.2	0.05%	[126, 142]
Seo et al. [146]	Model Hyperloop	0.0014 - 0.0028	0.47-0.93	34%	N/A
Hruschka and Klatt [147]	Projectile in Tube	0.52 - 1.6	0.5 - 1.5	39%	N/A

Table 2: Experimental validation cases commonly used in numerical Hyperloop studies.

4.6. Validation

There is currently very little published experimental data for the flow generated by a Hyperloop. This hinders the validation of the numerical methods used to simulate the aerodynamics. To adequately validate a numerical method for simulating a Hyperloop, each of the following fundamental flow characteristics should be considered:

1. Transonic flow,
2. Blockage effects,
3. Shock reflections,
4. Low Reynolds number.

Experimental testing of a Hyperloop-type system which combines these features is non-trivial due to the unconventional flow regimes. The low Reynolds number needs to be achieved by reducing the air pressure or using very small-scale models, both of which are difficult to achieve experimentally. The Mach number and blockage ratio, on the other hand, need to match that expected in a full-scale ETT system to accurately capture the transonic and blockage effects. Further difficulties also arise in obtaining the correct ground/tube motion relative to the pod. This problem has been the subject of much discussion in the context of conventional train experiments [3, 130], with solutions that include moving model tests and translating-ground wind tunnel tests.

In the numerical studies discussed here, validation was either neglected or completed indirectly using experimental cases that share similarities to Hyperloop (with varying degrees of relevance). No single validation case (other than a specific Hyperloop experiment) is likely to combine all of the fundamental flow features. In the absence of this, various cases should be tested to ensure that each flow characteristic is considered and some indication should be given for the level of accuracy acquired. Table 2 summarises the experimental studies that have been used most widely as validation in Hyperloop research, including the relevant flow properties in each case.

4.7. Experimental Data

The only experimental aerodynamics published on a Hyperloop-type system to date was recently undertaken by Seo et al. [146]. They investigated a 1:15 scale simplified axisymmetric model moving through a tube with a blockage ratio of 34%. The ambient pressure in the tube was reduced to 150Pa and the flow was choked for all runs.

The model was propelled by the sudden release of a high-pressure air tank. It then travelled through a diffusion tank where the propulsion air is bled off, before entering the tube test section. This method allowed the model to reach up to Mach 0.93, which is well within the intended design range for a full scale Hyperloop. The issue with this method is that the model has to enter the test-section from the larger diffusion tank, and generates pressure waves in the process. This is similar to the waves generated when a high-speed train enters a tunnel [3, 65]. A full-scale Hyperloop will be sealed within the tube the whole time it is in motion, and so these entrance waves will not be generated. Also, the air expelled during the acceleration process of the experiment isn't perfectly diffused away and thus a flow is induced in the test section. The authors do account for this with an estimation of the induced flow velocity when comparing their results with the 1D theory.

Pressures were measured at static points along the length of the test section, over the full time that the model is in the tube. From this data, the propagation speed and intensity of the shock waves generated in front of the model were calculated (the waves behind the model were not investigated). These were found to be in good agreement with predictions from 1D theory for the characteristics of the shock wave generated by the choked flow (see section 4.3 and [85]). This suggests that the entrance waves did not have too significant of an effect on the characteristics of the choked flow shock wave.

The ambient pressure achieved within the tube (150Pa) is within the range that is proposed for a full scale Hyperloop. The leading shock propagation speed, which was the focus of this research, can be shown to be independent of the ambient tube pressure using the 1D equations (section 4.3 and [85]). However, the combination of the reduced scale and reduced pressure give a diameter-based Reynolds number of 2,800 at the fastest test speed. This is around a factor of 10 lower than a full scale Hyperloop. It may therefore have been more realistic to choose pressure in such a way that the Reynolds number was matched to the full scale. This would have given the correct boundary layer characteristics and thus friction drag (though these were not the focus of this study and were not measured).

This research represents an important first step in the experimental study of the flow characteristics of ETT. Further research is required to fully explore the different flow regimes and provide rigorous benchmarks for validating theoretical and numerical studies. The most important future directions for experimental ETT research include:

1. Investigation of the drag properties of the pod across the different flow regimes,
2. Measurements of surface pressure on the pod,

3. Studies of the boundary layer characteristics (including transition and separation),
4. Analysis of the dependence of the flow on ambient pressure and temperature conditions in the tube.

5. Flow States and Aerodynamic Characteristics

5.1. Expected Flow States

The expected flow in the ETT system can be separated into the choked and unchoked regimes, which can then be divided further into 6 distinct states based on the pod speed. The flow states discussed here are based on a combination of results from the literature. The primary basis is Hruschka and Klatt [147], who studied the related case of a blunt projectile fired at transonic speeds in a tube (28% blockage ratio). They proposed and investigated the flow states both experimentally and numerically. The trends in flow characteristics are also supported by the 1D theory in section 4.3 and in [91]. They have also been observed in CFD simulations [39, 85, 127, 123, 141] and an experimental study of ETT systems [146]. All of the individual flow features are well understood from fundamental aerodynamics theory, and are observed in classical problems such as converging-diverging ducts and free jet flows [86].

The flow states for increasing pod speed and a given blockage ratio are shown in figure 8. The isentropic and Kantrowitz limits are also included, which divide the flow state space into the choked and unchoked regimes. The expected flow states are:

- A) Subsonic Incompressible Flow:** In this regime, the pod Mach number is low enough that the flow does not exhibit strong compressibility effects. Weak compression waves will be sent upstream of the pod at approximately sonic speed [147]. A full-scale Hyperloop is unlikely to have a cruising speed low enough to be in this flow state.
- B) Subsonic Compressible Flow:** For higher subsonic speeds, the compression waves ahead of the pod will be steepened and coalesce into a normal shock wave. This process is also observed for high-speed trains in tunnels, and is described in more detail by [66, 95, 148]. The separation distance between this leading shock wave and the front of pod will increase with time [85]. The local flow around the pod (behind the leading shock) will be approximately steady and isentropic.
- *) The Isentropic Limit (Subsonic):** The approximate critical Mach number at which the flow through the throat becomes sonic and mass flow rate past the pod is limited.
- C) Underdeveloped Choked Flow:** Once the speed passes the critical Mach number (subsonic branch of the isentropic limit), mass is continually accumulated upstream of the pod. The overall flow is inherently unsteady

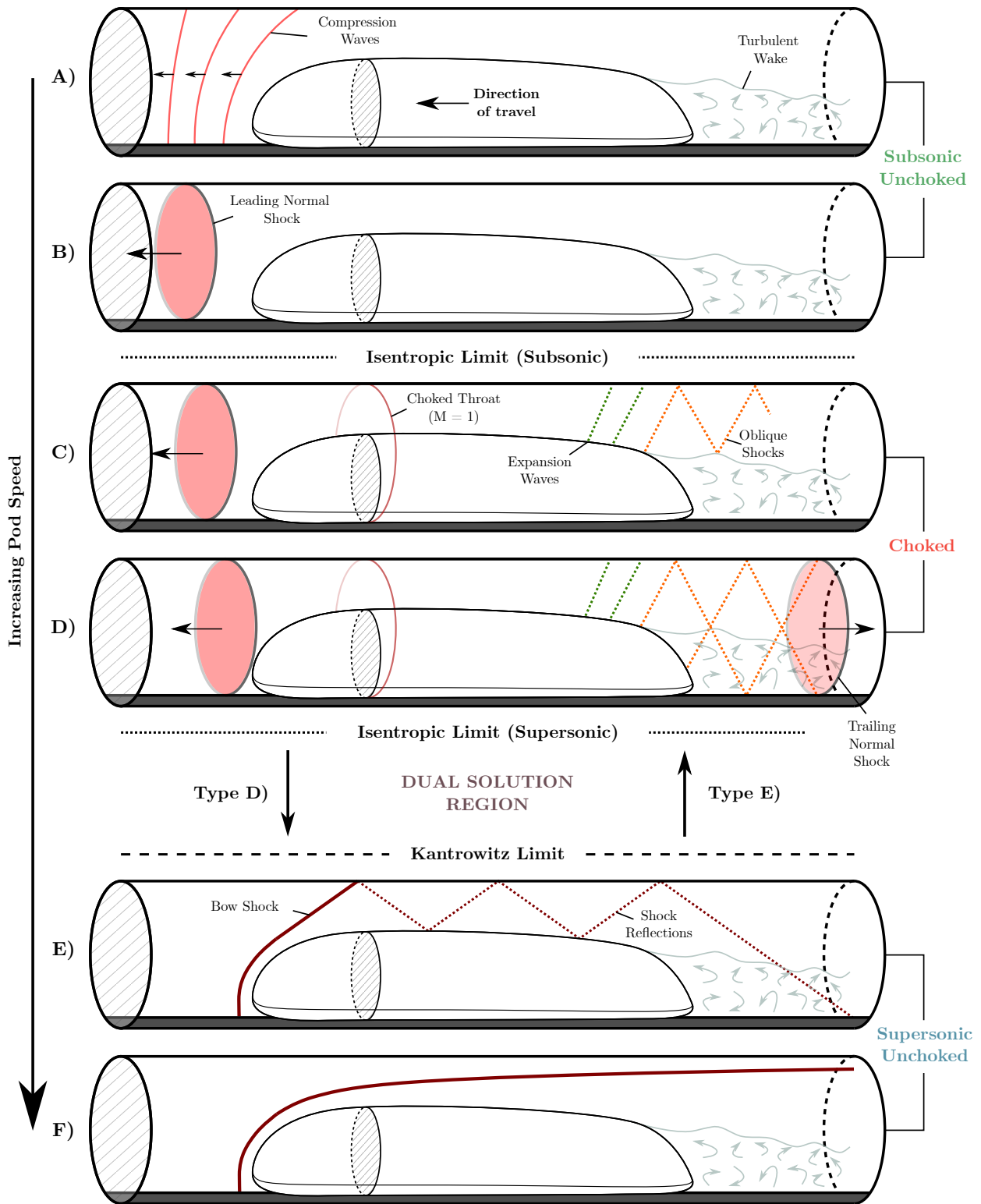


Figure 8: Approximate flow states of a Hyperloop for increasing pod speed (with a fixed blockage ratio).

and the drag experienced by the pod increases with time. Expansion waves are produced in the supersonic region toward the tail where the pod-tube gap diverges. Oblique shocks are then generated where the free-stream supersonic flow is turned into itself by the separated wake region. These shocks reflect off the walls and the wake flow before dissipating [85, 149].

D) Fully Developed Choked Flow: Further speed increase causes the oblique shocks to enter the wake flow, which becomes fully developed with a regular pattern of reflecting shock diamonds filling the whole tube diameter [85, 125]. The oblique shocks no longer dissipate smoothly. Instead, a trailing normal shock is generated where the pressure must rapidly increase at the end of the wake region to match the far-field tube pressure [123]. As with the leading shock, in pod fixed co-ordinates, this trailing shock travels away from the pod with time. With increasing speed, the rate at which the leading normal shock separates from the pod is reduced, while the separation rate for the trailing shock is increased [39]. The local flow around the pod (behind the leading shock and in front of the trailing shock) can still be taken as quasi-steady [97, 123]

* **The Isentropic Limit (Supersonic):** This is the lowest supersonic Mach number above which unchoked flow can exist. If the flow is decelerating from higher speeds (with the flow unchoked), this is therefore the point at which the flow chokes again.

D/E) Dual Solution: Both choked and unchoked flow can exist in this regime. The flow will remain choked (type D) while accelerating from lower speeds into this regime, up to the Kantrowitz limit. The flow will remain unchoked (type E) while decelerating from higher speeds into this regime, down to the supersonic isentropic limit.

* **The Kantrowitz Limit:** If the flow is accelerating from lower speeds with the flow choked, this is the Mach number at which the leading normal shock sits steady in relation to the pod.

E) Unchoked Flow with Strong Reflections: Beyond the Kantrowitz limit, the separation between the leading shock and the pod decreases and eventually the flow will unchoke again. The mass flow rate past the pod can be increased above the choked value and overall steady flow is possible. For relatively blunt pod geometries, the leading shock becomes a curved bow shock sitting off the nose, which reflects at the tube walls [127]. If the nose geometry is sharper, an attached oblique shock will be generated at the nose instead [92]. Depending on the strength of the reflecting shocks, it may be the case that a trailing normal shock is again generated where the pressure increases at the end of the wake region.

F) Unchoked Flow with Minimal Reflections: At very high speeds, the leading shock at the nose will not reflect

off the tube in the vicinity of the pod (aside from in the small gap underneath, depending on the pod height). The pod therefore experiences little blockage effect from the tube and the local flow is similar to that of the motion in free air. It is unlikely that this would be a feasible regime for ETT as the speeds would need to be excessively high, or the blockage ratio excessively low.

Ultimately, the blockage ratio will determine the range of pod speeds for which the flow is in each of the given states. For higher blockage ratios, the flow will transition from states A - C at lower pod speeds, and will transition from states C - E at higher speeds. The flow will therefore be choked over a greater range of operating speeds.

5.2. Aerodynamic Drag

The aerodynamic drag experienced by the Hyperloop pod will be highly dependant on the flow state. The typical expected profiles of the drag force and coefficient against Mach number are given in figure 9a. These plots are based on the results of a number Hyperloop CFD simulations [38, 40, 41, 63, 85, 91, 92, 125] and although the general features of the graphs are observed in each of the studies, the exact profiles are determined by the pod shape, blockage ratio and the tube pressure.

In subsonic unchoked flow (states A + B), the drag and drag coefficient both rise with Mach number. Once the flow becomes choked (state C), this rate of drag increase becomes much steeper due to mass accumulation and the associated pressure drag increase. After the choked flow becomes fully developed (state D), the gradient in the drag force becomes shallower. The drag increases at a slower rate than the square of the speed/Mach number, causing the drag coefficient to decrease with higher speed.

The expected drag characteristics for supersonic unchoked flow are not as well understood. This regime tends not to be investigated due to that fact that a high Mach number is needed for supersonic unchoked flow, even at moderate blockage ratios (see figure 6). From the limited literature, analysis of 1D [91] and 3D [92] results suggest that when the pods accelerates past the Kantrowitz limit, a rapid decrease in drag is observed as the flow becomes unchoked (with no normal shock upstream in the tube). Conversely, when a pod decelerates from high speeds where the flow is unchoked, the drag increases rapidly again at the supersonic isentropic limit. This is due to the flow re-choking and the leading normal shock being re-established upstream of the pod.

The drag profiles given in figure 9a and in the literature show the drag to be constant for a given Mach number. As discussed previously, this is not strictly the case when the flow is choked. Mass is accumulated upstream of the pod, causing the density and thus drag to increase continually. Most CFD studies are either taken to be steady, or transient with a very short simulation time (due to prohibitive computational cost) and therefore only a small set of instantaneous drag values can be obtained. The drag increase due to choking and mass accumulation over typical

journey timescales has not been quantified in the literature at the time of writing.

5.2.1. *Pressure vs Friction Drag*

Most of the drag experienced by the pod in an ETT system will be pressure drag, with a smaller contribution coming from friction drag [150]. The proportion of the overall drag coming from the pressure generally increases with Mach number, converging to a roughly constant value $>90\%$ once the flow is choked and fully developed [38, 85, 91, 150]. At very high speeds, the pressure drag will drop if the flow unchokes. The pressure contribution to the overall drag will also then reduce, and the friction drag may become the dominant contributor in this regime [91]. This profile is seen in a representative plot of the ratio of pressure drag to total drag in figure 9a.

5.2.2. *Blockage Ratio and Tube Pressure*

The drag profile of a pod will be heavily influenced by the blockage ratio and internal tube pressure [30]. The general effect of increasing blockage ratio can be seen in figure 9b, with the drag coefficient increasing across the full range of Mach numbers. Higher blockage ratios also change the positions of the isentropic and Kantrowitz limits, causing the flow to choke earlier and unchoke later (as predicted by the 1D theory). The rapid rise and peak in drag coefficient associated with choked flow is therefore observed at lower Mach numbers, while the drag reduction in unchoked flow is pushed to higher Mach numbers [40, 92].

A number of CFD investigations [30, 41, 133, 150, 151, 152] have also shown that the drag force experienced by a Hyperloop pod increases with higher internal tube pressure across all realistic speed regimes. Most of the studies find the relationship between drag force and tube pressure to be approximately linear, and the transition points between the flow states to be consistent between different internal pressures. As the pressure is proportional to the density, a linear drag force to pressure relationship suggests that the drag coefficient profile for a given pod and blockage ratio will be independent of the tube pressure.

5.3. *Number of Dimensions and Simulation Method*

When modelling ETT aerodynamics, the prediction of the flow states and transition points will depend on the dimension and method of simulation. Jang et al. [85] found the critical Mach number (i.e the point at which the flow chokes) in 2D Navier-Stokes CFD simulations to be higher than that predicted by the isentropic limit from 1D theory. They attributed this to the previously discussed fact that 1D theory does not predict a leading shock below the isentropic limit, across which the flow velocity is reduced. The flow will only choke once the velocity behind this leading shock reaches the critical value, and so the pod can travel at higher speeds without choking. This delayed choking effect was however not observed in 3D simulations near the isentropic limit performed by Yu et al. [127].

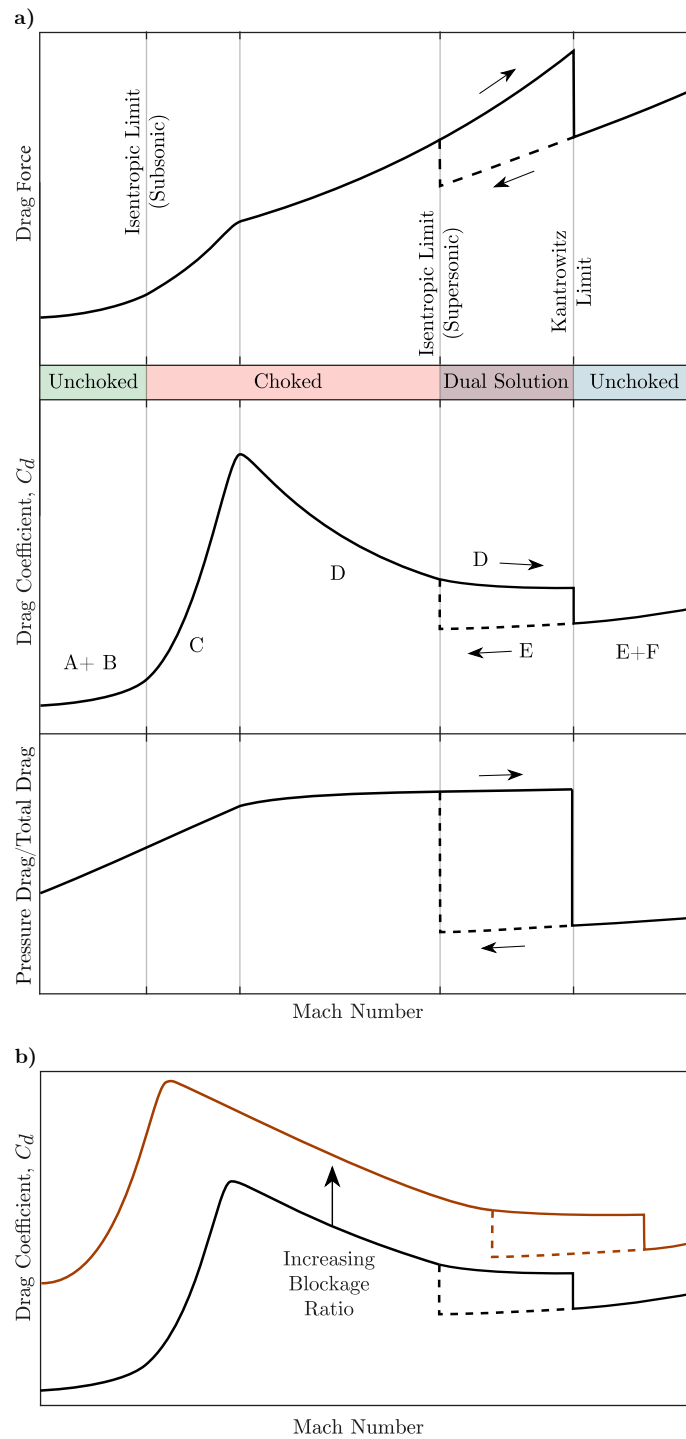


Figure 9: (a) Generalised profiles of drag force and drag coefficient for a Hyperloop pod with a given tube pressure and blockage ratio [38, 40, 41, 63, 85, 91, 92, 125]. (b) Effect of the blockage ratio on the expected drag coefficient profile. Dashed lines denote drag characteristics for unchoked flow in the dual solution region. The letters correspond to the 6 flow states shown in figure 8.

This may be due to the fact that these simulations were performed in pod-fixed coordinates, while those of Jang et al. [85] used a more realistic moving-model approach in absolute coordinates.

Jang et al. [85] found that the presence of the leading shock, which increases the critical Mach number, had a greater impact than the reduced effective blockage ratio due to the boundary layers (which would act to decrease the critical Mach number). Thus, in general, higher-dimensional viscous methods were found to predict a higher Mach number at which the flow chokes compared to the 1D isentropic theory [85].

Kang et al. [40] compared the observed drag results between axisymmetric 2D simulations and the corresponding 3D simulations. They found the drag coefficient to be slightly increased in the 3D case. The shape of the drag coefficient profile was consistent between the two methods, suggesting that the predicted flow transition points are the same in 2D axisymmetric and 3D simulations, though this was not explicitly discussed.

More research is required to assess whether the flow transition points predicted by the 1D isentropic and Kantrowitz limits are accurate enough for ETT design purposes. This would involve comprehensive simulation of the system in both 2D and 3D across a broad spectrum of blockage ratios and Mach numbers. From here, it can be determined whether 1D and 2D methods concur with full 3D predictions of the choked and unchoked regimes. If the isentropic and Kantrowitz limits are not sufficient, more accurate equations for the transition Mach numbers could be generated (as functions of the blockage ratio).

5.4. Acceleration

In much of the research on ETT, numerical simulations are performed in steady-state, or with the pod instantaneously accelerated to its final speed. Comparisons to simulations with realistic acceleration and deceleration phases have shown this instantaneous startup condition to be reasonable [153]. This is due to the fact that once a constant speed is reached, the flow quickly develops into an approximately steady-state (locally) and the drag experienced by the pod becomes relatively stable (though it can increase with running time if the flow is choked). The developing flow field in the accelerating and decelerating stages are expected to exert strong and rapidly-changing forces on the pod due to the formation and breakdown of shocks in the system [136, 153]. The drag force on the pod will be higher in the deceleration phase than in the acceleration phase (for the same speed) as a result of the mass accumulation ahead of the pod. The drag experienced will also be higher for greater acceleration magnitudes [136].

6. Design Considerations

The evacuated tube transport concept contains a vast number of design parameters which would need to be investigated and optimised in order to design a viable system. Only a handful of parameters have been investigated in the literature thus far. These are summarised in figure 10 and discussed in the following subsections.

6.1. Pod Shape

The shape of a Hyperloop pod will have a significant impact on the aerodynamic characteristics of the system. The nose and tail geometries of a pod have been investigated by a number of authors with the objective of minimising drag and, in some cases, optimising lift. The range of geometries that have been considered include simplified axisymmetric shapes [38, 41, 92, 127] through to full 3D shape optimisation [132]. In the majority of these studies, the main body of the pod is taken to be cylindrical. The effects of changing the nose and tail geometries on the aerodynamics have been found to be largely independent of each other over a range of speed regimes [92, 132]. This allows more efficient shape-optimisation by considering the nose and tail separately, and combining the optimal shapes into a final geometry.

For speeds below the isentropic limit, Zhou et al. [92] and Kim and Oh [132] found the most significant drag reduction can be achieved by optimising the shape of the pod tail. Both studies found a long, sharp tail to be the optimum shape. Le et al. [138] also studied the effect of tail length for choked flow speeds. Again, they found that longer tail geometries resulted in lower overall drag. They also observed a significant effect of the tail length on the structure of the oblique shock wave generated at the rear of the pod. Shorter tails produced a pair of shocks from the upper and lower surfaces of the pod, whereas longer tails did not produce an oblique shock at the upper surface due to the more gradual geometry change. Consequently, fewer shock interactions and reflections are observed for longer tails, giving a simpler flow pattern behind the pod.

At speeds above the Kantrowitz limit, Zhou et al. [92] found that lengthening the nose of the pod gave the greatest drag reduction. This was due to the increase in sharpness which reduces the angle, and thus the strength, of the oblique shock generated at the nose. However, for much lower speeds with unchoked flow and no shock generation at the head of the pod, Kim and Oh [132] found a more blunt nose to be optimal in their study.

In the choked flow regime, it has been observed in axisymmetric simulations that the length and shape of the nose and tail have a lesser effect on the drag of the pod [92, 124]. However, Hu et al. [123] still found a significant drag decrease (up to 9%) for longer nose/tail geometries in choked flow using high-fidelity simulations with realistic tube positioning. This was due to the longer nose generating a leading shock with a slower separation speed relative to the pod, giving a shorter disturbed high-pressure region in front of the pod. They also investigated the differences in the vortex structure of the wake flows, finding a longer tail to give the smallest wake, which had less prominent interaction with the oblique shocks. This also contributed to the reduced drag.

Le et al. [138, 154] investigated the effect of the pod nose and tail angle on the aerodynamic characteristics. They considered upward, downward and neutral angles as shown in figure 10b. The angle was referred to as the slope in the original study, though this term is not used here to avoid confusion with the curvature of the pod. They found

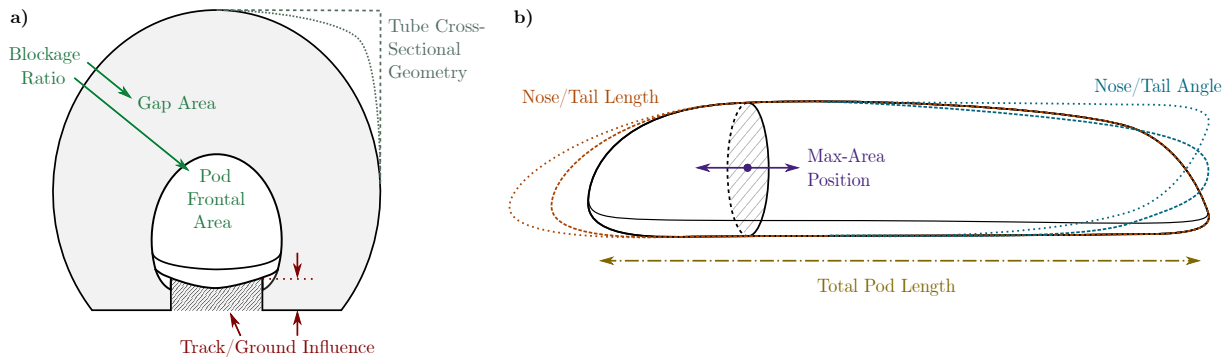


Figure 10: Front (a) and side (b) views of design parameters for the ETT concept that have been investigated in the literature: total pod length [38, 41], nose/tail length [92, 123, 155], nose/tail geometry and slope [124, 132, 138, 154], track/ground influence [120, 132, 126], blockage ratio [40, 30, 92], maximum-area position [36, 37] and tube geometry [156].

that having upward or downward nose/tail angles had minimal effect on the drag across a wide range of speeds. This gives further evidence to suggest that the drag is chiefly dependent on the blockage ratio and 1D profile of the gap area between the pod and tube, which was consistent between the different angled designs. Overall it was seen that a neutral angle on the nose and tail (i.e. an axisymmetric pod) minimised the drag, but this result may not generalise to the case where the pod is not centred radially within the tube. Their results did however show that the angle, particularly of the tail, had a significant effect on the lift of the pod at speeds above 200 m/s. Downward angled geometries produced positive lift, while upward angles caused negative lift. Some amount of positive lift could be beneficial for the ETT system, to complement the suspension system. However, high lifting loads or a strong dependence of the lift on the pod speed would be undesirable, and potentially dangerous.

6.2. Pod Length

Numerical investigations [38, 41] using a large range of pod lengths (11-86 m) have been performed to investigate the impact on the aerodynamics of the system. It was found that increasing the pod length has little effect on the pressure drag, but increases the friction drag proportionally. As the pressure drag is by far the more dominant contribution, particularly when the flow is choked, the length of the pod only has a small effect on the total drag it will experience. If the pod can travel at very high speeds where the flow unchokes, the overall drag will be more sensitive to pod length, as the contribution of the friction drag will be proportionately higher.

6.3. Tube Shape

Most studies in the literature assume a circular cross section for the tube. This is the most simple geometry, but may not give the best performance. Wang et al. [156] have presented the only study of the effect of the tube shape on the aerodynamics. They simulated the system with 3 different tube cross-sectional geometries: circular, square

and arched. They found the square-sectioned tube to minimise the drag experienced by the pod, though this was only tested at a single blockage ratio and speed. Further investigation is required to optimise the cross-sectional shape of the tube for ETT. This will need to consider the full range of potential speeds and blockage ratios, along with the structural characteristics of the tube and its ability to sustain the forces caused by the low internal pressure.

6.4. *Optimisation*

Much of the literature on ETT aerodynamics is focused on the need for optimising various parameters in the system. As noted previously, the most important objective for optimisation of the ETT system is drag; significantly lower drag is the fundamental principle that gives ETT potentially vast benefits compared to traditional modes of transport. The full optimisation of ETT is, however, a multi-objective problem, as considerations will also need to be made for the lift, side-forces, aerodynamic moments and energy requirements. Many combinations of these objectives are likely to be in conflict and thus a systematic approach is needed to consider the trade-offs and find optimal designs [3].

To date, the majority of the ETT research has been performed using parametric studies. This involves performing simulations (or experiments) for a set of values of a design variable and monitoring the sensitivity of the output (e.g. the drag). This has given some initial insight into how individual parameters affect the performance of the ETT system, however there is a need for more sophisticated optimisation studies to understand the interaction of different design variables and their influence on the various objective functions. There are many suitable design optimisation methods, all of which aim to achieve this in a systematic way and minimise number of the simulations/experiments required [3].

The first step for an optimisation usually involves a Design of Experiments (DoE), which is a systematic method of selecting design points in the parameter space [157]. Once the chosen design points have been evaluated with CFD simulations, a metamodel can be produced which approximates the behaviour of the system. There are many methods of building metamodels (e.g. polynomial regression, Kriging, radial basis functions [157]), all of which give a model that can be used to estimate of the value of the objective functions at any given design point, without requiring a direct simulation (as this is expensive). From here, an optimisation algorithm can be used to optimise the objective functions on the metamodel to find predictions for optimal designs. This process can then be repeated by simulating these design points and feeding the results back into the metamodel until adequate results are obtained. Again, there is a wealth of numerical optimisation schemes that are commonly used, including genetic algorithms [158, 159] and differential evolution algorithms [35, 160].

A key advantage of design optimisation is that a problem formulation which covers a wide design space can lead to non-intuitive design philosophies with the potential for vastly improved performance. For a given problem, the

greater the number of design variables, the larger the design space will be. Unfortunately, this leads to the ‘curse of dimensionality’, whereby higher dimensional space requires significantly more data from a large number of design evaluations. In the context of Hyperloop, the need for 3D high-fidelity CFD simulations exacerbates this issue; without a large enough number of solutions, the objective function landscape is insufficiently covered and regions of favourable design can be missed.

Another issue in CFD-based design optimisation is that numerical noise can be present, which in turn can hinder optimisation searches [161]. Gilkeson et al. [161] quantified numerical noise and proposed strategies to help mitigate against this in a low-speed vehicle aerodynamics problem. One such strategy is the implementation of noise-smoothing metamodels including the moving least squares method [162, 163].

Design optimisation has been used very successfully within the aerospace industry, including for relevant problems such as the shape design of high-speed trains in free-air [164, 165, 166] and when entering tunnels [159], along with the optimisation of components for supersonic land speed record vehicles [167, 168]. Thus far, design optimisation methods have been underutilised in Hyperloop aerodynamics research, with very few examples in the literature [35, 132]. Design optimisation offers significant potential for efficient investigation of the performance of the system across the full design space and could be highly valuable in realising a practical evacuated tube transport system.

6.5. Deceleration and Braking

For a Hyperloop vehicle to operate at high speeds it will of course need to decelerate at the end of a journey. Achieving this through aerodynamic means presents another challenge due to the low density gas required in the tube. Potentially, momentary increases in the blockage could exploit choking to dramatically raise drag and slow the vehicle sufficiently (provided that this could be done in a stable fashion) [169]. The concept of using aerodynamic brakes for supersonic ground vehicles has received some attention in the design of Bloodhound LSR [170]. Whether this could safely be incorporated into the design of a vehicle operating in confined spaces remains an open question.

A separate issue concerning deceleration relates to the physiological effects on humans. When rapidly decelerating a vehicle, the Somatogravic illusion can be extremely unpleasant. This occurs when there is conflict in the human brain brought about by differences in visual reference and the vestibular system which is responsible for balance. When Richard Noble set the world land speed record piloting Thrust 2 in 1983, parachutes were used to exploit aerodynamic braking to reduce the vehicle speed from 650 mph to 200 mph. During these 5.5g deceleration events, Noble felt as though he was hurtling downwards toward the centre of the Earth, which was a frightening experience [171]. With the Hyperloop concept in mind, the Somatogravic illusion must be a consideration, regardless of the means of deceleration, whether aerodynamic or otherwise.

6.6. Boundary Layer Transition

As the flow in the ETT system is at low Reynolds number, the aerodynamic characteristics will be more sensitive to boundary layer transition than conventional high-speed vehicles (e.g. trains in tunnels). Transition was considered in the design process by two of the teams competing in the SpaceX Hyperloop competition [36, 37]. Both teams focused their designs on encouraging early boundary layer transition by having the maximum sectional area toward the front of the pod. The idea behind this is that the turbulent boundary layer can tolerate higher adverse pressure gradients without separation, which would increase the pressure drag significantly. The trade off with this design principle is that friction drag is increased when a higher proportion of the boundary layer is turbulent. However, this was found to have less impact than the drag increase caused by separation of the laminar boundary layer when transition was delayed. Forced transition of the boundary layer using a physical trip could potentially also be used to prevent separation for a given pod shape [36]. This has not yet been studied in the context of Hyperloop.

The SpaceX competition studies were at a reduced scale, with the tube diameter approximately 50% of a full size design [5, 172]. The Reynolds numbers, however, are approximately equal to those in a proposed commercial system as the pressure in the SpaceX test tube was higher [37]. Boundary layer transition effects have not yet been studied for a system at full commercial scale, though some authors have used transitional turbulence models to attempt to capture these effects [38, 120]. At present, no comprehensive assessment of the expected transition characteristics and the impact of these on the overall dynamics has been given for a full-scale Hyperloop design.

6.7. Ground Influence

Ground proximity, as illustrated in figure 10a, is an important factor in conventional train aerodynamics which influences the wake flow structure, along with the lift and drag forces [173]. For ETT, the ground effect will be altered by the enclosed tube environment as the pod has varying wall proximity in every direction. The transonic speeds and associated shock waves will also further complicate the ground interaction. A number of studies have investigated transonic ground effect in contexts such as confined projectiles [174] and land speed record vehicles [170]. It is found that shock generation, interaction and reflection causes a complex dependence of lift and drag characteristics on the proximity to the ground. This area has also been reviewed in detail by Doig [175], who notes that the rapid stability changes associated with transonic ground effect poses major challenges for maglev based vehicles like the Hyperloop, due to their high sensitivity to ground clearance.

As noted already, many computational Hyperloop studies neglect the influence of the ground clearance and geometry by assuming the pod to be radially centered in a circular tube. This simplifies the meshing process by avoiding small gaps between the pod and the tube, but will affect the accuracy and validity of the observed aerodynamic characteristics. Some investigations have attempted to minimise the effect of this simplification by matching their blockage

ratio to that of a realistic tube configuration with a flat base and low ground clearance [36, 132]. Kim and Oh [132] simulated both a simplified/centred geometry and the equivalent geometry with a realistic ground shape and positioning, finding 11% higher drag in the latter case. This difference is greater than the drag reduction they found through their 3D shape optimisation of the simplified centred geometry (8% reduction compared to the baseline design).

Zhou et al. [120] performed simulations of a Hyperloop under different ground clearances based on the realistic values for maglev suspension systems. They found within the small range of clearances (25 - 100mm) that the drag was fairly consistent but that lift increased with a decrease in separation. Hu et al. [126] studied a similar case, investigating the effect of including a realistic track geometry. Similarly, they found the inclusion of the track had little influence on drag forces, but that the lift coefficient increased by 23% compared to the case without the track.

The ground clearance and radial positioning of the pod are some of the most significant factors affecting the aerodynamic characteristics of the ETT system. Further research is required to fully understand and quantify the influence of ground effects, and this will need to include an evaluation across a range of speeds and flow regimes. The lift mechanisms are currently not well understood and this is a notable gap in knowledge.

6.8. Multiple Pods and Cross Passage

Though most Hyperloop studies have considered a single pod in the system, there will of course be multiple pods operating within the same tube. From the discussion so far, it has been shown that the flow field generated by each pod can cause disturbances to propagate at high speeds and for significant distances in both directions, particularly when the flow is choked. Therefore, it is likely that the local aerodynamic characteristics of each pod will be highly dependent on other pods nearby, with strong interactions between the respective flow fields.

Numerical research on the interaction of multiple pods travelling in the same direction [176, 177] has shown that when the flow is choked, the typical oblique shocks and trailing normal shock are not produced at the rear of the pod if another pod is travelling close behind. This would be beneficial, as a strong drag reduction of up to 60% is observed for the leading pod in comparison to an isolated pod [176]. The effect on the drag of the trailing pod in a multiple-pod system is much weaker, as the wake and trailing shock pattern remains relatively unchanged by the presence of the upstream pods. This is in contrast to the effects of drafting, which is common for conventional ground vehicles, where it is the trailing vehicles that can experience significantly reduced drag compared to the lead or an isolated vehicle.

The limitation of these findings is that only relatively short separation distances (40-150 m) were tested, which are unlikely to be safe due to the braking distance at such high speeds. More research is required to understand whether this drag reduction is observed with more realistic pod separation distances. The significant benefits of this 'platooning' concept for drag reduction has also been the subject of a large amount of research on trucks and other road vehicles [178, 179].

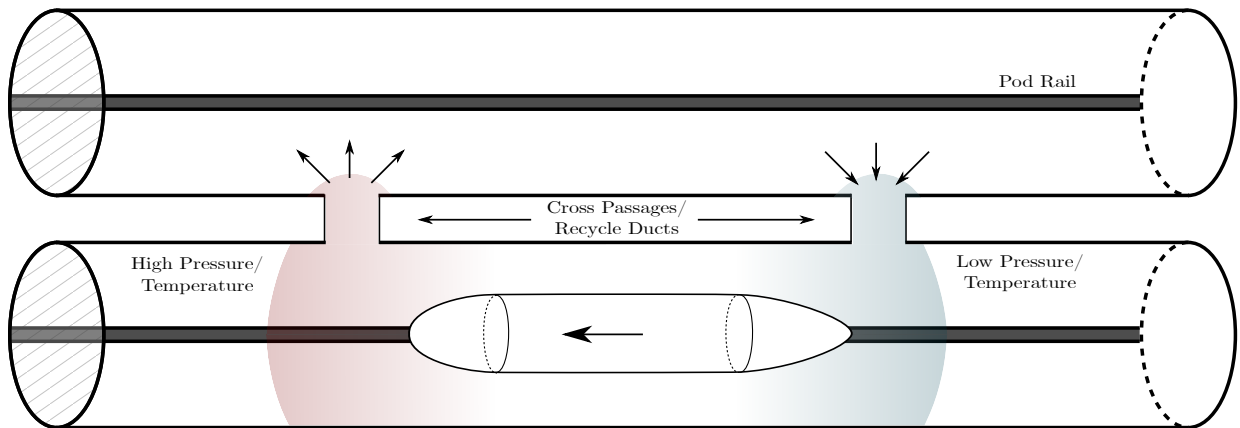


Figure 11: Aerial view showing the concept of cross passages to reduce drag and extreme temperatures by allowing air exchange between multiple ETT tubes coupled together.

The effect of directly coupling the pods together has also been tested [176], and was found to reduce the average drag-per-pod even more significantly (a further 15%) compared to the case where the pods just travel close together. Where possible, coupling the pods in this way could therefore be a good way to improve the aerodynamic efficiency of the system, though it is likely to reduce the frequency of the service and thus the convenience for passengers.

The effect of cross passages/recycle ducts has also been studied for ETT [142, 180, 181]. This involves ducts which couple two or more ETT tubes together, e.g. for pods travelling in opposite directions as in figure 11. The idea behind this is to alleviate the piston effect and reduce extreme pressures and temperatures by allowing airflow between the two tubes. In turn this should reduce the drag in the system.

Using numerical simulations, cross passages have been found to reduce the peak drag coefficient experienced by the pod by up to 80%, while the maximum temperature at the nose can be reduced by 25% and the minimum value in the wake increased by 23% [142]. The effectiveness of cross passages improves with higher blockage ratios and train speeds, while increasing the number and the size of the ducts also increases effectiveness [180, 181].

While cross passages may offer a viable way to reduce the drag and extreme temperatures in an ETT system, they do bring significant disadvantages. Coupling tubes together means that if the vacuum were to fail in one tube, both would become unusable. It has also been found that the interaction of the pods in the opposing tubes can cause highly complex and potentially unpredictable flows, giving strong lateral forces which could cause the pods to shake violently left to right [142].

6.9. Bleed Systems

The discussion in the previous sections has shown that the flow is likely to be choked over much of the realistic speed range of ETT. To mitigate the effect of upstream mass accumulation and the rising drag associated with choking,

it has been proposed that a bleed system could be used in each of the pods [5]. The idea of the bleed system is to draw in high-pressure air from the front of the pod and route this through to the low pressure region at the rear. This would increase the mass flow rate past the pod, alleviate the pressure build up, and allow a wider range of speeds without the flow choking.

A bleed system may be passive or active. A passive system would be driven solely by the pressure difference between the nose and tail, using ducting to transport the bleed air through the pod without additional energy input. An active system would incorporate a device to drive the system, which would require additional energy, and further increase the mass flow rate through the ducting. The original Hyperloop Alpha document [5] and most subsequent studies do not use the term bleed system. They instead specifically refer to an axial compressor, as used in aircraft gas turbines, to be the active means of reducing choking. Bleed system is the preferred term here, which includes both the ducting and potentially an active device to increase the mass flow. Also, the compression achieved by a gas turbine compressor is used to reduce the volume of the gas before combustion, which is then expanded to generate thrust. This is not required in the context of a Hyperloop pod and the device operates more as a pump rather than a compressor. A pump is therefore the more general and appropriate term for an active component incorporated into the bleed system.

Preliminary CFD investigations have been conducted for the aerodynamics of the system with an active bleed system incorporated in a pod [63, 182]. Bizzozero et al. [63] considered the bleed system using two different methods. First, incorporating additional source terms into the simulations and second, using fan interface type boundary conditions. Both of these methods modelled the compressed airflow the whole way through the pod. Lluesma-Rodríguez et al. [182] modelled the bleed system using a boundary condition at the nose to remove mass at a given pressure, which was then re-introduced using an inlet boundary condition at the tail. This method therefore ignores the air passage through the pod.

Both investigations compared the pressure distributions and the power consumption between cases with and without the bleed system using consistent blockage ratios. They observed that the bleed system was successful in reducing the pressure at the nose and preventing the flow from choking. Bizzozero et al. [63] found reductions in the power requirement of up to 44% by using the bleed system, while Lluesma-Rodríguez et al. [182] found up to 70% reductions. In the latter case, however, the volume taken up in the pod for transporting the bleed air was not included in the blockage ratio calculations. The cases with the bleed system therefore had a lower effective blockage ratio (and thus lower internal volume) compared to the cases without. This may account for a significant portion of the observed power reductions. The most significant power reduction was observed at the higher Mach numbers and blockage ratios (well above the subsonic isentropic limit) where the flow is strongly choked and the mass accumulation rate is

high. For cases with only weak or no choking, both investigations found the bleed system to be ineffective, causing a net increase in power consumption. A mechanism for shutting off the bleed system could therefore be advantageous for situations in which the pod travels at lower speeds.

Bizzozero et al. [63] found that both higher blockage ratios and higher Mach numbers required the active bleed system to run at a higher pressure ratio (defined by the ratio of the pressure immediately upstream to downstream) for greater efficiency. The study was however limited to modest pressure ratios (<4) due to numerical stability issues when this was increased. The results suggested that the most optimum pressure ratio would likely be higher than they could simulate for high speeds and blockage. They also investigated the generality and scalability of their results, finding that the power benefits of the bleed system were broadly independent of the tube pressure by testing at both 1000 Pa and 10 000 Pa. They also observed that these results were insensitive to the physical size of the system by comparing to simulations at half scale; this suggests that scale effects may be minimal.

Overall, the research suggests that the use of a bleed system on Hyperloop pods could be advantageous for reducing power consumption by avoiding flow choking. This would be achieved at high speeds and blockage ratios, which are the areas of the design space in which a feasible Hyperloop should sit. High speeds are integral to the concept and give the main benefit of Hyperloop over conventional rail, while high blockage ratios allow smaller tubes and thus lower construction costs and vacuum requirements.

Despite these encouraging signs, further research is required into the use of bleed systems. The current studies only consider speeds up to Mach 0.8, though a Hyperloop could be designed for higher cruising speeds. It is likely that the effectiveness of a bleed system would decrease for very high speeds, as the choking strength will be decreased when approaching the supersonic isentropic and Kantrowitz limits [127]. The use of bleed systems therefore needs to be investigated across the whole possible speed range of ETT.

The boundary conditions and geometries used to model the bleed system in the studies to date were also highly simplified, using 2D axisymmetry and either neglecting or simplifying the passage of the bleed air. Investigation of more realistic 3D geometries and careful consideration of the duct volume required to route the bleed air is therefore needed. Simulations capable of modelling higher pressure ratios would also be beneficial for understanding the optimum value of this parameter across a wider range of blockage ratios and speeds. Finally, it is worth noting that only active bleed systems have been considered in the literature, despite the fact that a passive bleed system would be simpler to implement and would not require additional energy input. Therefore, an important question for future investigation is whether passive systems could sufficiently reduce flow choking without overly decreasing the blockage ratio, as they would be preferable if this is the case.

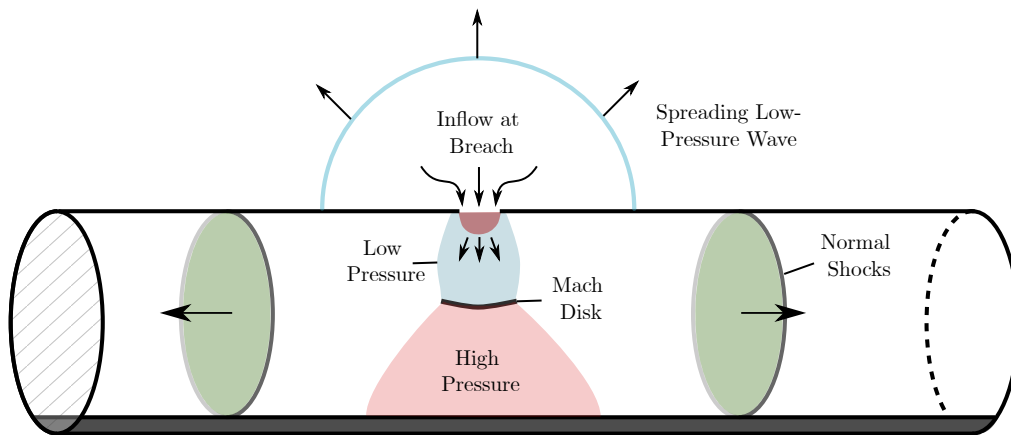


Figure 12: Schematic of the impinging underexpanded jet flow generated by a breach in the tube. Adapted from [148, 183]

6.10. Tube Breaches

One potential issue with the ETT concept is the possibility of breaches in the tube causing a breakdown of the sealed environment. In this situation, the pressure difference between the tube and the external environment would cause a flow from the ambient surroundings into the tube. This could be caused in a variety of ways, including physical damage to the tube (e.g from extreme weather, natural disasters, terrorism) or failure of the sealing mechanisms.

If the tube operates at the proposed 100 Pa [5, 148, 183], the magnitude of the pressure difference to the external environment could cause very high inflow rates, even for the smallest of breaches. Ahn et al. [183] numerically studied the flow generated by breaches of different diameters from 0.01 m to 0.9 m. They found that the mass flow rate into the tube, \dot{m} , was approximately linear with the area of the breach, A_b :

$$\dot{m} = 208.2A_b. \text{ (kg/s)} \quad (6.1)$$

The induced flow was found to reach very high velocity, up to Mach 4.5 near the breach [183]. The flow structure is observed to be that of a highly underexpanded jet [148], which is a widely observed flow in engineering applications with free jets [184, 185]. A schematic of the jet in the tube is shown in figure 12. The incoming air is accelerated to supersonic speeds and a normal shock is generated, known in this case as a Mach disk, which slows the flow to subsonic conditions and increases the pressure. The jet then impinges on the tube and spreads along the walls. For larger breaches with high enough mass flow rate, two normal shocks are generated which span the full cross-section of the tube and travel away from the breach in each direction [183]. The strength and propagation speed of these shocks increases with the size of the breach [148].

Kim et al. [148] performed numerical simulations and 1D theoretical analysis of an ETT system with a breached

tube. They studied the interaction of the normal shocks generated by the breach and by the pod in choked flow. The shocks are reflected and their strength changed at any point where they interact with the pod, the breach, or another shock. This therefore creates a highly complex dynamic pressure field of interacting shocks. They observed that drag increases rapidly when the shocks from the breach interact with the pod, and that a strong normal force is exerted on the pod as it passes the breach.

The Mach number of the shocks generated by the breach, M_b , was evaluated in 1D using shock fixed coordinates, in a similar way to how the upstream shock speed is calculated in choked flow (see section 4.3 and [85]). The equation can be formulated as a function of the mass flow rate into the breach, \dot{m}_{breach} ,

$$\frac{\dot{m}_{\text{breach}}}{2} = \rho_2 u_2 A_{\text{tube}} = A_{\text{tube}} \frac{\rho_1 (\gamma + 1) M_s}{(\gamma - 1) M_s^2 + 2} \sqrt{\frac{(\gamma - 1) M_s^2 + 2}{2\gamma M_s^2 - (\gamma - 1)}} \sqrt{\frac{\gamma R [(\gamma - 1) M_s^2 + 2] [2\gamma M_s^2 - (\gamma - 1)]}{(\gamma + 1)^2 M_s^2}}, \quad (6.2)$$

where subscripts 1 and 2 denote conditions ahead of (i.e further from the breach) and behind the shock respectively. The factor of 1/2 applied to the mass flow rate in the above equation accounts for the fact that two identical shocks are generated in the tube, travelling in opposite directions away from the breach. The mass flow rate can be calculated based on the area of the breach

$$\dot{m}_{\text{breach}} = A_{\text{breach}} p_0 \sqrt{\frac{\gamma}{RT_0}} \left(\frac{\gamma + 1}{2} \right)^{\frac{\gamma+1}{2(\gamma-1)}}. \quad (6.3)$$

Again, subscript 0 is used for total quantities. Equations 6.2 and 6.3 can then be solved along with the isentropic and normal shock relations (equations 4.3 - 4.7, 4.12) in shock-fixed coordinates, to give the propagation speed of the shocks due to the breach.

If the flow is choked, the isentropic equations can be used to predict the local flow properties everywhere in the domain, and the pressure can be integrated over the pod surface to give an estimation of the drag. This gives the characteristics for short flow times before the breach shock waves interact with the shocks and flow generated by the pod. Similar formulations of the above equations can then be used to calculate the properties after these interactions. Kim et al. [148] found their 1D theoretical results for the wave propagation speed and tube pressures derived in this way gave excellent agreement with 2D planar CFD simulations.

6.11. Temperature and Mach Number

As already discussed, flow choking presents a significant challenge to the viability of ETT. The onset of this phenomenon is dictated by the critical Mach number in the throat between the pod and the tube. Equation 4.4 shows that the local speed of sound is dependent on the ambient temperature and in hotter conditions, the speed of sound

($M = 1$) is faster. Therefore, with a given Mach number, high-speed vehicles such as Hyperloop can potentially travel faster if the ambient temperature is increased. Alternatively, for a given pod velocity, changing the temperature of the surrounding gas would serve to change the Mach number, which could be used to reduce the drag or potentially alleviate choking onset.

This concept was used to the advantage of a team of engineers who broke the world land speed record in 1983 [171, 186]. They designed, built and operated Thrust 2, a ground vehicle powered by a jet engine. This vehicle was attempting to break a long-standing speed record of 622 mph set by Blue Flame, a rocket powered car, in 1970. In order to set a new record, Thrust 2 needed to exceed the 622 mph mark by at least 1%, averaged over two one-mile runs, each in opposite directions, and within one hour. The driver, Richard Noble, preferred to run the vehicle early in the morning on location in Black Rock Desert, Nevada. Due to the limited power and shape of Thrust 2, transonic drag rises meant that the vehicle could not exceed Mach 0.84 [171, 186], and it could not achieve the record. However, the chief designer, John Ackroyd, realised that running Thrust 2 in the hottest part of the day raised the local speed of sound; the vehicle subsequently broke the land speed record, setting a mark of 633mph with a peak speed of 651 mph [171]. Their calculations showed that at $M = 0.834$ the vehicle speed could be raised from 623 mph at 6°C to 649 mph at 28°C, a notable difference [186].

The potential for reducing drag by controlling the tube ambient temperature in a Hyperloop system has been studied numerically [38, 187]. Bao et al. [187] found a 40% reduction in drag when comparing an initial tube temperature of -30°C to 120°C in their simulations at 1000 km/h. This was due to higher temperatures causing a much shorter wake with weaker shock patterns due to the increased speed of sound. Oh et al. [38] observed similar findings when testing across a range of pod speeds. They saw a drag reduction of up to 20% when increasing the ambient tube temperature from 2°C to 100°C, but did not include any analysis of the flow field and the cause of the drag reduction.

The results from the operation of Thrust 2 and the numerical studies on Hyperloop systems underline the importance of vehicle speed and its relationship to ambient air temperature. Clearly this has the potential to be advantageous for Hyperloop, by reducing the drag experienced by the pod. None of the current studies have directly investigated whether flow choking could be delayed by temperature increases, so further research on this question and its impact is required. Despite the potential benefits, increasing the temperature of a low-density gas could also prove to be extremely challenging and energy intensive. Furthermore, a high ambient temperature in the tube could cause safety issues and would require further energy for cooling the pods to maintain passenger comfort.

Numerical studies on the heat transfer characteristics of ETT have shown the expected temperature fields to be highly complex, owing to the generation and reflection of shocks, and their interaction with the boundary layer and wake flows [39, 87, 125, 141, 188, 189]. The most significant source of heating in the system is due to friction at

the pod surface [141], which generates high temperature gradients in the boundary layer. This aerodynamic heating is relatively mild when the flow is in the subsonic unchoked regime, but becomes much more severe if the flow is supersonic [141]. Higher blockage ratios also increase the temperatures in the system, particularly if the flow chokes [39]. In choked flow, the viscous heating at the pod walls is exacerbated by the heating due to high pressure in the choked region around the pod. In numerical simulations, peak surface temperatures on the pod have been observed up to 250°C around the nose [141] and as low as -180°C around the tail [188]. Such extreme temperatures are observed in the operation of supersonic jets, where they are known to cause significant stresses and accelerated aging of the aircraft structure [190]. Careful structural design and material selection will therefore be needed for the Hyperloop pods to account for this extreme operating environment.

7. Conclusions and Future Directions

A significant amount of research into evacuated tube transport aerodynamics has been conducted, which has allowed the prediction of the fundamental flow characteristics of the system. The different flow states of the ETT system have been quantified, based on the blockage ratio and the Mach number. The isentropic and Kantrowitz limits have also been derived from 1D theory as predictors of the transition points between the choked and unchoked regimes.

Investigations have shown that pressure drag dominates the resistance experienced by the ETT pod, particularly when the flow is choked, and the blockage ratio (which determines the choking points) is by far the biggest influence on the drag of the pod. Lower drag is achieved with smaller blockage ratios, though the larger required tube size is undesirable in terms of construction and vacuum costs. Initial studies on optimising the pod shape for reduced drag have revealed that longer nose and tail geometries are favourable, while the length of the pod is relatively insignificant. In-depth study of optimal pod shape is needed, as most current work looks at either highly simplified geometries, or shapes taken directly from high-speed trains. This is unlikely to be optimal in the ETT system due to the vastly different flow regimes. Design optimisation studies across much more open sets of design parameters are also necessary to allow a more comprehensive exploration of the possible design space for the ETT pod. These should include multi-objective studies, which account for conflicting objectives such as lift, side-loads and aerodynamic moments, along with drag and energy needs.

Thus far, the research on ETT aerodynamics has almost exclusively been based on numerical simulation, utilising 1D isentropic methods and 2D/3D Navier-Stokes CFD. There is now a critical requirement for more experimental research on the aerodynamics of ETT. The findings of the numerical simulations need to be validated against real-world data in order to have confidence in the results. However, obtaining high-quality experimental data is difficult,

due to the unconventional flow regimes of ETT. The low Reynolds number, high Mach number, and relative motion of the pod and tube all pose significant challenges for designing experiments to accurately analyse the flow in the system.

Further key deficiencies in ETT aerodynamics knowledge, which could form immediate future directions of the research, include:

1. The influence of the clearance between the pod and the tube walls. Many studies use axisymmetric simulations with the pod radially centred and floating in the tube despite this being an unrealistic simplification.
2. The significance of mass accumulation and the associated drag increase due to flow choking over time. Transient simulations of the system have so far been limited to short time scales (<10 s). The magnitude and severity of the drag rise over time has therefore not yet been quantified.
3. Optimising the cross-sectional shapes of both the tube and the main body of the pod. These fundamental parameters are likely to have a strong effect on the aerodynamics, while also influencing the structural characteristics in response to the pressure differences and the usable volume inside the pod.
4. Boundary layer transition effects and the drag trade-offs between designing for earlier or later transition. This has not yet been fully discussed for a full-scale system. The use of physical trips to transition the boundary layer at a chosen point on the pod could also be explored.
5. Methods of mitigating or delaying flow choking. The use of a bleed system is one such method, which has been the subject of some preliminary investigations. More research is required to demonstrate the feasibility of using a bleed system to mitigate choking without negating the benefits by requiring high additional energy consumption.

Overall, evacuated tube transport presents a promising area of research that has the potential to enable efficient and sustainable high-speed travel. The concept is, however, still in its infancy and a significant amount of research is required to refine the design. Novel and innovative techniques in aerodynamic design will be required to overcome the significant hurdles in realising a practical system and achieving the theoretical benefits of ETT.

Acknowledgements

This work was supported by the UK Engineering and Physical Sciences Research Council (EPSRC) grant EP/S022732/1 for the University of Leeds Centre for Doctoral Training in Fluid Dynamics. The authors thank I. Tristante for suggestions of corrections and improvements of the review.

References

- [1] International Energy Agency, World Energy Outlook 2021, 2021. URL: <https://iea.org/reports/world-energy-outlook-2021>.
- [2] International Energy Agency, Net Zero by 2050, 2021. URL: <https://iea.org/reports/net-zero-by-2050>.
- [3] C. Baker, T. Johnson, D. Flynn, H. Hemida, A. Quinn, D. Soper, M. Sterling, Train Aerodynamics: Fundamentals and Applications, Butterworth-Heinemann, 2019. doi:10.1016/B978-0-12-813310-1.12001-5.
- [4] Hyperloop One, Hyperloop One Home Page, 2023. URL: <https://hyperloop-one.com/>, accessed: 03-10-2023.
- [5] E. Musk, Hyperloop Alpha, 2013. URL: https://tesla.com/sites/default/files/blog_images/hyperloop-alpha.pdf.
- [6] K. Decker, J. Chin, A. Peng, C. Summers, G. Nguyen, A. Oberlander, G. Sakib, N. Sharifrazi, C. Heath, J. Gray, R. Falck, Conceptual feasibility study of the Hyperloop vehicle for next-generation transport, in: 55th AIAA Aerospace Sciences Meeting, 2017. doi:10.2514/6.2017-0221.
- [7] A. S. Abdelrahman, J. Sayeed, M. Z. Youssef, Hyperloop Transportation System: Analysis, Design, Control, and Implementation, IEEE Transactions on Industrial Electronics 65 (2018) 7427–7436. doi:10.1109/TIE.2017.2777412.
- [8] E. Chaidez, S. P. Bhattacharyya, A. N. Karpetis, Levitation methods for use in the hyperloop high-speed transportation system, Energies 12 (2019). doi:10.3390/EN12214190.
- [9] H. W. Lee, K. C. Kim, J. Lee, Review of maglev train technologies, IEEE Transactions on Magnetics 42 (2006) 1917–1925. doi:10.1109/TMAG.2006.875842.
- [10] W. Y. Ji, G. Jeong, C. B. Park, I. H. Jo, H. W. Lee, A Study of Non-Symmetric Double-Sided Linear Induction Motor for Hyperloop All-In-One System (Propulsion, Levitation, and Guidance), IEEE Transactions on Magnetics 54 (2018). doi:10.1109/TMAG.2018.2848292.
- [11] S. Y. Choi, C. Y. Lee, J. M. Jo, J. H. Choe, Y. J. Oh, K. S. Lee, J. Y. Lim, Sub-sonic linear synchronous motors using superconducting magnets for the hyperloop, Energies 12 (2019). doi:10.3390/EN12244611.
- [12] M. Flankl, T. Wellerdieck, A. Tüysüz, J. W. Kolar, Scaling laws for electrodynamic suspension in high-speedtransportation, IET Electric Power Applications 12 (2018) 357–364. doi:10.1049/IET-EPA.2017.0480.
- [13] J. Lim, C. Y. Lee, J. H. Lee, W. You, K. S. Lee, S. Choi, Design model of null-flux coil electrodynamic suspension for the hyperloop, Energies 13 (2020). doi:10.3390/EN13195075.
- [14] J. Lim, C. Y. Lee, S. Choi, J. H. Lee, K. S. Lee, Design optimization of a 2G HTS magnet for subsonic transportation, IEEE Transactions on Applied Superconductivity 30 (2020). doi:10.1109/TASC.2020.2977037.
- [15] S. Choi, M. Cho, J. Lim, Electromagnetic drag forces between HTS magnet and tube infrastructure for hyperloop, Scientific Reports 13 (2023) 1–20. doi:10.1038/s41598-023-39916-7.
- [16] E. Tramacere, M. Pakštys, R. Galluzzi, N. Amati, A. Tonoli, T. A. Lembke, Modeling and experimental validation of electrodynamic maglev systems, Journal of Sound and Vibration 568 (2024) 117950. doi:10.1016/J.JSV.2023.117950.
- [17] R. B. Prosser, Medhurst, George (1759–1827), 2004. doi:10.1093/ODNB/9780192683120.013.18493.
- [18] H. O. Hardenberg, The middle ages of the internal-combustion engine, 1794-1886, Society of Automotive Engineers, 1999.
- [19] R. A. Buchanan, The Atmospheric Railway of I. K. Brunel, Social Studies of Science 22 (1992) 231–243.
- [20] R. H. Goddard, The Limit of Rapid Transit, Scientific American 101 (1909) 366.
- [21] R. L. Forgacs, Evacuated Tube Vehicles Versus Jet Aircraft for High-Speed Transportation, Proceedings of the IEEE 61 (1973) 604–616. doi:10.1109/PROC.1973.9117.
- [22] I. G. Macola, Timeline: tracing the evolution of hyperloop rail technology, 2021. URL: <https://railway-technology.com/features/timeline-tracing-evolution-hyperloop-rail-technology/>.

- [23] M. Jufer, F.-L. Perret, F. Descocudres, Y. Trotet, Swissmetro, an Efficient Intercity Subway System, *Structural Engineering International* 3 (1993) 184–189. doi:10.2749/101686693780607921.
- [24] A. Rudolf, Simulation of Compressible Flow in Tunnel Systems Induced by Trains Traveling at High Speed, Ph.D. thesis, EPFL Thesis No. 1806, 1998.
- [25] A. Cassat, Swissmetro – Project Development Status, in: *Proceedings of International Symposium on Speed-up Service Technology for Railway and Maglev Systems, STECH'03*, 2003, pp. 453 – 460.
- [26] SwissMetro-NG, SwissMetro-NG Home Page, 2022. URL: <https://swissmetro-ng.org/>, accessed: 09-03-2022.
- [27] D. Oster, M. Kumada, Y. Zhang, Evacuated tube transport technologies (ET3): a maximum value global transportation network for passengers and cargo, *Journal of Modern Transportation* 19 (2011) 42–50. doi:10.3969/j.issn.2095-087X.2011.01.007.
- [28] ET3 Global Alliance Inc., Evacuated Tube Transport Technologies – 'Space travel on Earth', 2022. URL: <http://et3.com/>, accessed: 20-03-2022.
- [29] H. Bi, B. Lei, Aerodynamic characteristics of evacuated tube high-speed train, in: *Proceedings of the 2nd International Conference on Transportation Engineering, ICTE 2009*, American Society of Civil Engineers (ASCE), 2009, pp. 3736–3741. doi:10.1061/41039(345)616.
- [30] T. K. Kim, K. H. Kim, H. B. Kwon, Aerodynamic characteristics of a tube train, *Journal of Wind Engineering and Industrial Aerodynamics* 99 (2011) 1187–1196. doi:10.1016/j.jweia.2011.09.001.
- [31] Y. Zhang, Numerical simulation and analysis of aerodynamic drag on a subsonic train in evacuated tube transportation, *Journal of Modern Transportation* 20 (2012) 44–48. doi:10.1007/bf03325776.
- [32] Z. Tang, J. Qin, J. Sun, The aerodynamics analysis and optimization design of evacuated tube transportation, *Sensors and Transducers* 158 (2013) 414–420.
- [33] J. Ma, D. Zhou, L. Zhao, Y. Zhang, Y. Zhao, The approach to calculate the aerodynamic drag of maglev train in the evacuated tube, *Journal of Modern Transportation* 21 (2013) 200–208. doi:10.1007/S40534-013-0019-6.
- [34] X. Chen, L. Zhao, J. Ma, Y. Liu, Aerodynamic simulation of evacuated tube maglev trains with different streamlined designs, *Journal of Modern Transportation* 20 (2012) 115–120. doi:10.1007/BF03325788.
- [35] J. Braun, J. Sousa, C. Pekardan, Aerodynamic design and analysis of the hyperloop, *AIAA Journal* 55 (2017) 4053–4060. doi:10.2514/1.J055634.
- [36] M. M. J. Opgenoord, P. C. Caplan, Aerodynamic Design of the Hyperloop Concept, *AIAA Journal* 56 (2018) 4261–4270. doi:10.2514/1.J057103.
- [37] N. Nick, Y. Sato, Computational fluid dynamics simulation of Hyperloop pod predicting laminar–turbulent transition, *Railway Engineering Science* 28 (2020) 97–111. doi:10.1007/s40534-020-00204-z.
- [38] J. S. Oh, T. Kang, S. Ham, K. S. Lee, Y. J. Jang, H. S. Ryu, J. Ryu, Numerical analysis of aerodynamic characteristics of Hyperloop system, *Energies* 12 (2019) 518. doi:10.3390/en12030518.
- [39] Y. Sui, J. Niu, Q. Yu, Y. Yuan, X. Cao, X. Yang, Numerical analysis of the aerothermodynamic behavior of a Hyperloop in choked flow, *Energy* 237 (2021). doi:10.1016/J.ENERGY.2021.121427.
- [40] H. Kang, Y. Jin, H. Kwon, K. Kim, A study on the aerodynamic drag of transonic vehicle in evacuated tube using computational fluid dynamics, *International Journal of Aeronautical and Space Sciences* 18 (2017) 614–622. doi:10.5139/IJASS.2017.18.4.614.
- [41] T. T. G. Le, K. S. Jang, K.-S. Lee, J. Ryu, Numerical Investigation of Aerodynamic Drag and Pressure Waves in Hyperloop Systems, *Mathematics* 8 (2020). doi:10.3390/MATH8111973.
- [42] D. Tudor, M. Paolone, Optimal Design of the Propulsion System of a Hyperloop Capsule, *IEEE Transactions on Transportation Electrifica-*

- tion 5 (2019) 1406–1418. doi:10.1109/TTE.2019.2952075.
- [43] D. Tudor, M. Paolone, Operational-driven optimal-design of a hyperloop system, *Transportation Engineering* 5 (2021). doi:10.1016/J.TRENG.2021.100079.
- [44] D. P. Connolly, P. K. Woodward, HeliRail: A railway-tube transportation system concept, *Transportation Engineering* 1 (2020). doi:10.1016/J.TRENG.2020.100004.
- [45] Swisspod, Swisspod Home Page, 2022. URL: <https://swisspod.ch/>, accessed: 20-03-2022.
- [46] Hyperloop Transportation Technologies, HyperloopTT Home Page, 2022. URL: <https://hyperlooptt.com/>, accessed: 20-03-2022.
- [47] Hardt Hyperloop, Hardt Hyperloop Home Page, 2022. URL: <https://hardt.global>, accessed: 20-03-2022.
- [48] Zeleros, Zeleros Hyperloop Home Page, 2022. URL: <https://zeleros.com/>, accessed: 20-03-2022.
- [49] Eurotube, Eurotube Home Page, 2022. URL: <https://eurotube.org/>, accessed: 20-03-2022.
- [50] Korea Railroad Research Institute, KKRI Major Research Technologies, 2022. URL: https://krri.re.kr/html/en/sub03/sub03_0301.html, accessed: 20-03-2022.
- [51] TransPod, TransPod Test Facility, 2022. URL: <https://transpod.com/test-facility/>, accessed: 20-03-2022.
- [52] L. Mitropoulos, A. Kortsari, A. Koliatos, Hypernex Deliverable D 2.1 Observatory Results, 2021. URL: <http://hypernex.industriales.upm.es/documents-and-results/>.
- [53] NOAA-S/T-76-1562, U.S. Standard Atmosphere, Standard, National Oceanic and Atmospheric Administration, 1976.
- [54] P. B. S. Lissaman, Low-Reynolds-Number Airfoils, *Annual Review of Fluid Mechanics* 15 (1983) 223–239. doi:10.1146/annurev.fl.15.010183.001255.
- [55] J. Keogh, G. Doig, S. Diasinos, N. Ryde, N. South, W. Australia, Flow compressibility effects around an open-wheel racing car, *The Aeronautical Journal* 118 (2014) 1409–1431. doi:10.1017/S0001924000010125.
- [56] E. M. Purcell, Life at low Reynolds number, *American Journal of Physics* 45 (1977) 3–11. doi:10.1119/1.10903.
- [57] W. Shyy, Y. Lian, J. Tang, D. Viieru, H. Liu, *Aerodynamics of Low Reynolds Number Flyers*, Cambridge University Press, 2007. doi:10.1017/CB09780511551154.
- [58] R. K. Singh, M. R. Ahmed, M. A. Zullah, Y. H. Lee, Design of a low Reynolds number airfoil for small horizontal axis wind turbines, *Renewable Energy* 42 (2012) 66–76. doi:10.1016/J.RENENE.2011.09.014.
- [59] W. J. Koning, W. Johnson, H. F. Grip, Improved Mars Helicopter Aerodynamic Rotor Model for Comprehensive Analyses, *AIAA Journal* 57 (2019) 3969–3979. doi:10.2514/1.J058045.
- [60] M. Anyoji, D. Numata, H. Nagai, K. Asai, Effects of Mach Number and Specific Heat Ratio on Low-Reynolds-Number Airfoil Flows, *AIAA Journal* 53 (2015) 1640–1654. doi:10.2514/1.J053468.
- [61] B. H. Carmichael, Low Reynolds number airfoil survey, volume 1, Technical Report, NASA CR-165803, 1981.
- [62] T. J. Mueller, S. M. Batill, Experimental Studies of Separation on a Two-Dimensional Airfoil at Low Reynolds Numbers, *AIAA Journal* 20 (1982) 457–463. doi:10.2514/3.51095.
- [63] M. Bizzozero, Y. Sato, M. A. Sayed, Aerodynamic study of a Hyperloop pod equipped with compressor to overcome the Kantrowitz limit, *Journal of Wind Engineering and Industrial Aerodynamics* 218 (2021) 104784. doi:10.1016/J.JWEIA.2021.104784.
- [64] J. Niu, Y. Sui, Q. Yu, X. Cao, Y. Yuan, Aerodynamics of railway train/tunnel system: A review of recent research, *Energy and Built Environment* 1 (2020) 351–375. URL: <https://doi.org/10.1016/j.enbenv.2020.03.003>. doi:10.1016/j.enbenv.2020.03.003.
- [65] M. S. Howe, The compression wave produced by a high-speed train entering a tunnel, *Proceedings of the Royal Society of London. Series A: Mathematical, Physical and Engineering Sciences* 454 (1998) 1523–1534. doi:10.1098/RSPA.1998.0220.
- [66] K. Takayama, A. Sasoh, O. Onodera, R. Kaneko, Y. Matsui, Experimental investigation on tunnel sonic boom, *Shock Waves* 5 (1995)

127–138. doi:10.1007/BF01435520.

- [67] U.S. Department of Transportation, *Subway Environmental Design Handbook Volume I: Principles and Applications*, Technical Report, 1976.
- [68] D. Cross, B. Hughes, D. Ingham, L. Ma, Enhancing the piston effect in underground railway tunnels, *Tunnelling and Underground Space Technology* 61 (2017) 71–81. doi:10.1016/J.TUST.2016.10.001.
- [69] C. J. Kirkland, *Engineering the Channel Tunnel*, CRC Press, 1995. doi:10.1201/9781482271157.
- [70] S. Matsuo, An overview of the Seikan tunnel project, *Tunnelling and Underground Space Technology* 1 (1986) 323–331. doi:10.1016/0886-7798(86)90015-5.
- [71] R. Simoni, Gotthard base tunnel, Switzerland – The world’s longest railway tunnel, *Proceedings of the Institution of Civil Engineers: Civil Engineering* 167 (2014) 159–166. doi:10.1680/CIEN.14.00001.
- [72] DB ProjektBau, *Technische Innovationen am Katzenbergtunnel*, 2011.
- [73] G. Mancini, A. Malfatti, Full scale measurements on high speed train Etr 500 passing in open air and in tunnels of Italian high speed line, *TRANSAERO — A European Initiative on Transient Aerodynamics for Railway System Optimisation* (2002) 101–122. doi:10.1007/978-3-540-45854-8{_}9.
- [74] A. E. Vardy, Unsteady Airflows in Rapid Transit Systems Part I: Measurements on the London Transport Victoria Line, *Proceedings - Institution of Mechanical Engineers* 194 (1980) 341–348. doi:10.1243/PIME{_}PROC{_}1980{_}194{_}040{_}02.
- [75] F. Wang, M. Weng, K. Xiong, J. Han, I. Obadi, F. Liu, Study on aerodynamic pressures caused by double-train tracking operation in a metro tunnel, *Tunnelling and Underground Space Technology* 123 (2022) 104434. doi:10.1016/j.tust.2022.104434.
- [76] T. Gilbert, C. J. Baker, A. Quinn, Gusts caused by high-speed trains in confined spaces and tunnels, *Journal of Wind Engineering and Industrial Aerodynamics* 121 (2013) 39–48. doi:10.1016/j.jweia.2013.07.015.
- [77] J. Y. Kim, K. Y. Kim, Experimental and numerical analyses of train-induced unsteady tunnel flow in subway, *Tunnelling and Underground Space Technology* 22 (2007) 166–172. doi:10.1016/J.TUST.2006.06.001.
- [78] L. Zhang, M. z. Yang, J. q. Niu, X. f. Liang, J. Zhang, Moving model tests on transient pressure and micro-pressure wave distribution induced by train passing through tunnel, *Journal of Wind Engineering and Industrial Aerodynamics* 191 (2019) 1–21. doi:10.1016/J.JWEIA.2019.05.006.
- [79] Q. S. Yang, J. H. Song, G. W. Yang, A moving model rig with a scale ratio of 1/8 for high speed train aerodynamics, *Journal of Wind Engineering and Industrial Aerodynamics* 152 (2016) 50–58. doi:10.1016/J.JWEIA.2016.03.002.
- [80] S. Saito, M. Iida, H. Kajiyama, Numerical Simulation of 1-D Unsteady Compressible Flow in Railway Tunnels, *Journal of Environment and Engineering* 6 (2011). doi:10.1299/jee.6.723.
- [81] P. Ricco, A. Baron, P. Molteni, Nature of pressure waves induced by a high-speed train travelling through a tunnel, *Journal of Wind Engineering and Industrial Aerodynamics* 95 (2007) 781–808. doi:10.1016/j.jweia.2007.01.008.
- [82] U.S Department of Transportation, *Aerodynamic Assessment and Mitigation – Design Considerations for High-Speed Rail*, 2022.
- [83] W. G. Vincenti, C. H. Kruger, *Introduction to Physical Gas Dynamics*, John Wiley, London, 1965.
- [84] M. A. Saad, *Compressible Fluid Flow*, Prentice-Hall Inc., 1985.
- [85] K. S. Jang, T. T. G. Le, J. Kim, K. S. Lee, J. Ryu, Effects of compressible flow phenomena on aerodynamic characteristics in Hyperloop system, *Aerospace Science and Technology* 117 (2021) 106970. doi:10.1016/J.AST.2021.106970.
- [86] J. D. Anderson, *Fundamentals of Aerodynamics*, 6 ed., McGraw-Hill, 2016.
- [87] Y. Sui, J. Niu, Y. Yuan, Q. Yu, X. Cao, D. Wu, X. Yang, An Aerothermal Study of Influence of Blockage Ratio on a Supersonic Tube Train System, *Journal of Thermal Science* 29 (2020) 1–12. doi:10.1007/S11630-020-1281-7.

- [88] NACA, Equations, tables, and charts for compressible flow, NACA-TR-1135 (1953).
- [89] D. M. Van Wie, F. T. Kwok, R. F. Walsh, Starting characteristics of supersonic inlets, 32nd Joint Propulsion Conference and Exhibit (1996). doi:10.2514/6.1996-2914.
- [90] A. Kantrowitz, C. D. Donaldson, Preliminary Investigation of Supersonic Diffusers, Technical Report, NACA-ACR-L5D20, 1945.
- [91] Z. Hou, Y. Zhu, J. Bo, A quasi-one-dimensional study on global characteristics of tube train flows, *Physics of Fluids* 34 (2022) 26104. doi:10.1063/5.0080544.
- [92] Z. Zhou, C. Xia, X. Du, X. Shan, Z. Yang, Impact of the isentropic and Kantrowitz limits on the aerodynamics of an evacuated tube transportation system, *Physics of Fluids* 34 (2022) 066103. doi:10.1063/5.0090971.
- [93] V. I. Zvegintsev, S. O. Morozov, D. G. Nalivaychenko, Gas dynamics of the uniform body acceleration in the channel, in: *AIP Conference Proceedings*, volume 2027, American Institute of Physics Inc., 2018. doi:10.1063/1.5065106.
- [94] M. Janić, Estimation of direct energy consumption and CO₂ emission by high speed rail, transrapid maglev and hyperloop passenger transport systems, *International Journal of Sustainable Transportation* 15 (2021) 696–717. doi:10.1080/15568318.2020.1789780.
- [95] J. E. A. John, T. Keith, *Gas Dynamics*, 3 ed., Pearson, 1969.
- [96] T. Li, J. Song, X. Zhang, Jiye Zhang, Weihua Zhang, Theoretical and numerical studies on compressible flow around a subsonic evacuated tube train, *Proceedings of the Institution of Mechanical Engineers, Part C: Journal of Mechanical Engineering Science* 236 (2022) 8261–8271. doi:10.1177/09544062221087826.
- [97] A. G. Hammit, Aerodynamic Analysis of Tube Vehicle Systems, *AIAA Journal* 10 (1972) 282–290. doi:10.2514/3.6577.
- [98] W. A. Woods, C. W. Pope, A generalised flow prediction method for the unsteady flow generated by a train in a single-track tunnel, *Journal of Wind Engineering and Industrial Aerodynamics* 7 (1981) 331–360. doi:10.1016/0167-6105(81)90057-X.
- [99] A. E. Vardy, Aerodynamic drag on trains in tunnels. Part 2. Prediction and validation, *Proceedings of the Institution of Mechanical Engineers, Part F: Journal of Rail and Rapid Transit* 210 (1996) 39–49. doi:10.1243/PIME{_}PROC{_}1996{_}210{_}325{_}02.
- [100] Dundee Tunnel Research, ThermoTun, 2023. URL: <https://thermotun.com/>, accessed: 27-09-2023.
- [101] A. H. Shapiro, *The Dynamics and Thermodynamics of Compressible Fluid Flow (Volume 2)*, Ronald Press Company, 1954.
- [102] M. Abdulla, K. A. Juhany, A Rapid Solver for the Prediction of Flow-Field of High-Speed Vehicle Moving in a Tube, *Energies* 15 (2022) 6074. doi:10.3390/EN15166074.
- [103] A. Baron, M. Mossi, S. Sibilla, The alleviation of the aerodynamic drag and wave effects of high-speed trains in very long tunnels, *Journal of Wind Engineering and Industrial Aerodynamics* 89 (2001) 365–401. doi:10.1016/S0167-6105(00)00071-4.
- [104] A. E. Vardy, On the method of characteristics in highly compressible flows, in: *Proceedings of the 14th International Conference on Pressure Surges*, Eindhoven, The Netherlands, 2023.
- [105] A. Jameson, W. Schmidt, E. Turkel, Numerical solution of the Euler equations by finite volume methods using Runge Kutta time stepping schemes, in: *14th Fluid and Plasma Dynamics Conference*, American Institute of Aeronautics and Astronautics, Reston, Virginia, 1981. doi:10.2514/6.1981-1259.
- [106] A. E. Vardy, High-Speed Vehicles in Low-Pressure Tunnels—Influence of Choked Flows, *Applied Sciences* 13 (2023) 10314. doi:10.3390/app131810314.
- [107] F. R. Menter, Two-equation eddy-viscosity turbulence models for engineering applications, *AIAA Journal* 32 (1994) 1598–1605. doi:10.2514/3.12149.
- [108] F. R. Menter, P. E. Smirnov, T. Liu, R. Avancha, A One-Equation Local Correlation-Based Transition Model, *Flow, Turbulence and Combustion* 95 (2015) 583–619. doi:10.1007/s10494-015-9622-4.
- [109] R. B. Langtry, F. R. Menter, S. R. Likki, Y. B. Suzen, P. G. Huang, S. Völker, A Correlation-Based Transition Model Using Local

- Variables—Part II: Test Cases and Industrial Applications, *Journal of Turbomachinery* 128 (2006) 423–434. doi:10.1115/1.2184353.
- [110] F. R. Menter, R. Langtry, S. Völker, S. Völker, Transition Modelling for General Purpose CFD Codes, *Flow, Turbulence and Combustion* 77 (2006) 277–303. doi:10.1007/S10494-006-9047-1.
- [111] F. R. Menter, Review of the shear-stress transport turbulence model experience from an industrial perspective, *International Journal of Computational Fluid Dynamics* 23 (2009) 305–316. doi:10.1080/10618560902773387.
- [112] S. B. Pope, *Turbulent Flows*, Cambridge University Press, 2000. doi:10.1017/CB09780511840531.
- [113] D. C. Wilcox, *Turbulence Modeling for CFD*, DCW Industries, Inc., 2006.
- [114] F. R. Menter, R. B. Langtry, S. R. Likki, Y. B. Suzen, P. G. Huang, S. Völker, A Correlation-Based Transition Model Using Local Variables—Part I: Model Formulation, *Journal of Turbomachinery* 128 (2006) 413–422. doi:10.1115/1.2184352.
- [115] D. K. Walters, D. Cokljat, A Three-Equation Eddy-Viscosity Model for Reynolds-Averaged Navier–Stokes Simulations of Transitional Flow, *Journal of Fluids Engineering* 130 (2008). doi:10.1115/1.2979230.
- [116] J. van Ingen, A suggested semi-empirical method for the calculation of the boundary layer transition region, Technische Hogeschool Delft, Vliegtuigbouwkunde, Report VTH-74 (1956).
- [117] A. M. O. Smith, N. Gamberoni, Transition, Pressure Gradient and Stability Theory, Technical Report ES-26388, Douglas Aircraft Company (1956).
- [118] M. Drela, XFOIL: An Analysis and Design System for Low Reynolds Number Airfoils, in: *Low Reynolds Number Aerodynamics*, Proceedings of the Conference Notre Dame, Indiana, USA, 5–7 June, Springer, Berlin, Heidelberg, 1989, pp. 1–12. doi:10.1007/978-3-642-84010-4.
- [119] R. B. Langtry, F. R. Menter, Transition modeling for general CFD applications in aeronautics, in: *43rd AIAA Aerospace Sciences Meeting and Exhibit*, 2005, pp. 15513–15526. doi:10.2514/6.2005-522.
- [120] P. Zhou, D. Qin, J. Zhang, T. Li, Aerodynamic characteristics of the evacuated tube maglev train considering the suspension gap, *International Journal of Rail Transportation* (2021). doi:10.1080/23248378.2021.1885514.
- [121] P. R. Spalart, Detached-Eddy Simulation, *Annual Review of Fluid Mechanics* 41 (2009) 181–202. doi:10.1146/annurev.fluid.010908.165130.
- [122] S. Zhong, B. Qian, M. Yang, F. Wu, T. Wang, C. Tan, J. Ma, Investigation on flow field structure and aerodynamic load in vacuum tube transportation system, *Journal of Wind Engineering and Industrial Aerodynamics* 215 (2021). doi:10.1016/J.JWEIA.2021.104681.
- [123] X. Hu, Z. Deng, J. Zhang, W. Zhang, Aerodynamic behaviors in supersonic evacuated tube transportation with different train nose lengths, *International Journal of Heat and Mass Transfer* 183 (2022). doi:10.1016/J.IJHEATMASSTRANSFER.2021.122130.
- [124] J. Niu, Y. Sui, Q. Yu, X. Cao, Y. Yuan, X. Yang, Comparative numerical study of aerodynamic heating and performance of transonic hyperloop pods with different noses, *Case Studies in Thermal Engineering* 29 (2022). doi:10.1016/J.CSITE.2021.101701.
- [125] J. Niu, Y. Sui, Q. Yu, X. Cao, Y. Yuan, Numerical study on the impact of Mach number on the coupling effect of aerodynamic heating and aerodynamic pressure caused by a tube train, *Journal of Wind Engineering and Industrial Aerodynamics* 190 (2019) 100–111. doi:10.1016/J.JWEIA.2019.04.001.
- [126] X. Hu, Z. Deng, J. Zhang, W. Zhang, Effect of tracks on the flow and heat transfer of supersonic evacuated tube maglev transportation, *Journal of Fluids and Structures* 107 (2021). doi:10.1016/J.JFLUIDSTRUCTS.2021.103413.
- [127] Q. Yu, X. Yang, J. Niu, Y. Sui, Y. Du, Y. Yuan, Theoretical and numerical study of choking mechanism of fluid flow in Hyperloop system, *Aerospace Science and Technology* 121 (2022) 107367. doi:10.1016/J.AST.2022.107367.
- [128] K. Zhou, G. Ding, Y. Wang, J. Niu, Aeroheating and aerodynamic performance of a transonic hyperloop pod with radial gap and axial channel: A contrastive study, *Journal of Wind Engineering and Industrial Aerodynamics* 212 (2021) 104591. doi:10.1016/J.JWEIA.

2021.104591.

- [129] F. Moukalled, L. Mangani, M. Darwish, The characteristic boundary condition in pressure-based methods, *Numerical Heat Transfer, Part B: Fundamentals* 76 (2019) 43–59. doi:10.1080/10407790.2019.1644942.
- [130] H. B. Kwon, Y. W. Park, D. H. Lee, M. S. Kim, Wind tunnel experiments on Korean high-speed trains using various ground simulation techniques, *Journal of Wind Engineering and Industrial Aerodynamics* 89 (2001) 1179–1195. doi:10.1016/S0167-6105(01)00107-6.
- [131] H. A. Stine, K. Wanlass, M. Field, C. Washington, Theoretical and Experimental Investigation of Aerodynamic-heating and Isothermal Heat-transfer Parameters on a Hemispherical Nose with Laminar Boundary Layer at Supersonic Mach Numbers, *NACA Technical Note* 3344 (1954).
- [132] H. Kim, S. Oh, Shape optimization of a hyperloop pod's head and tail using a multi-resolution morphing method, *International Journal of Mechanical Sciences* 223 (2022) 107227. doi:10.1016/J.IJMECSCI.2022.107227.
- [133] Y. Sui, J. Niu, P. Ricco, Y. Yuan, Q. Yu, X. Cao, X. Yang, Impact of vacuum degree on the aerodynamics of a high-speed train capsule running in a tube, *International Journal of Heat and Fluid Flow* 88 (2021) 108752. doi:10.1016/J.IJHEATFLUIDFLOW.2020.108752.
- [134] R. Guerra, W. Waidmann, C. Laible, An experimental investigation of the combustion of a hydrogen jet injected parallel in a supersonic air stream, in: *AIAA 3rd International Aerospace Planes Conference*, 1991, American Institute of Aeronautics and Astronautics Inc, AIAA, 1991. doi:10.2514/6.1991-5102.
- [135] W. Waidmann, F. Alff, U. Brummund, W. Clauss, M. Oschwald, J. Sender, W. Waidmann, Experimental Investigation of the Combustion Process in a Supersonic Combustion Ramjet (SCRAMJET) Combustion Chamber, in: *Deutscher Luft- und Raumfahrtkongress, DGLR-Jahrestagung*, 1994.
- [136] J. Niu, Y. Sui, Q. Yu, X. Cao, Y. Yuan, X. Yang, Effect of acceleration and deceleration of a capsule train running at transonic speed on the flow and heat transfer in the tube, *Aerospace Science and Technology* 105 (2020) 105977. doi:10.1016/J.AST.2020.105977.
- [137] N. Li, J. T. Chang, K. J. Xu, D. R. Yu, W. Bao, Y. P. Song, Prediction dynamic model of shock train with complex background waves, *Physics of Fluids* 29 (2017) 116103. doi:10.1063/1.5000876.
- [138] T. T. G. Le, J. Kim, M. Cho, J. Ryu, Effects of tail shapes/lengths of Hyperloop pod on aerodynamic characteristics and wave phenomenon, *Aerospace Science and Technology* 131 (2022) 107962. doi:10.1016/J.AST.2022.107962.
- [139] B. U. Reinartz, C. D. Herrmann, J. Ballmann, W. W. Koschel, Aerodynamic Performance Analysis of a Hypersonic Inlet Isolator Using Computation and Experiment, *Journal of Propulsion and Power* 19 (2003) 868–875. doi:10.2514/2.6177.
- [140] C. D. Herrmann, W. W. Koschel, Experimental investigation of the internal compression of a hypersonic intake, in: *38th AIAA/ASME/SAE/ASEE Joint Propulsion Conference and Exhibit*, 2002. doi:10.2514/6.2002-4130.
- [141] Q. Yu, X. Yang, J. Niu, Y. Sui, Y. Du, Y. Yuan, Aerodynamic thermal environment around transonic tube train in choked/unchoked flow, *International Journal of Heat and Fluid Flow* 92 (2021) 108890. doi:10.1016/J.IJHEATFLUIDFLOW.2021.108890.
- [142] X. Hu, Z. Deng, W. Zhang, Effect of cross passage on aerodynamic characteristics of super-high-speed evacuated tube transportation, *Journal of Wind Engineering and Industrial Aerodynamics* 211 (2021). doi:10.1016/J.JWEIA.2021.104562.
- [143] T. Gao, J. Liang, M. Sun, Y. Zhao, Analysis of Separation Modes Variation in a Scramjet Combustor with Single-Side Expansion, *AIAA Journal* 55 (2017) 1307–1317. doi:10.2514/1.J055411.
- [144] T. Gao, J. Liang, M. Sun, Symmetric/asymmetric separation transition in a supersonic combustor with single-side expansion, *Physics of Fluids* 29 (2017) 126102. doi:10.1063/1.4990668.
- [145] L. D. Kayser, F. Whiton, Surface Pressure Measurements on a Boattailed Projectile Shape at Transonic Speeds, Technical Report, US Army Armament Research And Development Command ARBRL-MR-03161, 1982.
- [146] Y. Seo, M. Cho, D. H. Kim, T. Lee, J. Ryu, C. Lee, Experimental Analysis of Aerodynamic Characteristics in the Hyperloop System,

- Aerospace Science and Technology (2023) 108265. doi:10.1016/J.AST.2023.108265.
- [147] R. Hruschka, D. Klatt, In-pipe aerodynamic characteristics of a projectile in comparison with free flight for transonic Mach numbers, *Shock Waves* 29 (2019) 297–306. doi:10.1007/s00193-018-0816-2.
- [148] J. Kim, K. S. Jang, T. T. G. Le, K.-S. Lee, J. Ryu, Theoretical and numerical analysis of pressure waves and aerodynamic characteristics in Hyperloop system under cracked-tube conditions, *Aerospace Science and Technology* 123 (2022) 107458. doi:10.1016/J.AST.2022.107458.
- [149] P. Zhou, J. Zhang, T. Li, W. Zhang, Numerical study on wave phenomena produced by the super high-speed evacuated tube maglev train, *Journal of Wind Engineering and Industrial Aerodynamics* 190 (2019) 61–70. doi:10.1016/J.JWEIA.2019.04.003.
- [150] Z. Zhou, C. Xia, X. Shan, Z. Yang, Numerical Study on the Aerodynamics of the Evacuated Tube Transportation System from Subsonic to Supersonic, *Energies* 15 (2022) 3098. doi:10.3390/EN15093098.
- [151] F. Lluesma-Rodríguez, T. González, S. Hoyas, CFD simulation of a hyperloop capsule inside a closed environment, *Results in Engineering* 9 (2021). doi:10.1016/J.RINENG.2020.100196.
- [152] T. Ma, X. Hu, J. Wang, Y. Rao, J. Zheng, Z. Deng, Effect of air pressure on aerodynamic characteristics of the HTS maglev running in a tube, *IEEE Transactions on Applied Superconductivity* 31 (2021). doi:10.1109/TASC.2021.3099770.
- [153] H. Bi, Z. Wang, H. Wang, Y. Zhou, Aerodynamic phenomena and drag of a maglev train running dynamically in a vacuum tube, *Physics of Fluids* 34 (2022) 096111. doi:10.1063/5.0104819.
- [154] T. T. G. Le, J. Kim, K. S. Jang, K. S. Lee, J. Ryu, Numerical study on the influence of the nose and tail shape on the aerodynamic characteristics of a Hyperloop pod, *Aerospace Science and Technology* 121 (2022) 107362. doi:10.1016/J.AST.2022.107362.
- [155] X. Zhang, Y. Jiang, T. Li, Effect of Streamlined Nose Length on the Aerodynamic Performance of a 800 km/h Evacuated Tube Train, *Fluid Dynamics & Materials Processing* 16 (2020) 67–76. doi:10.32604/fdmp.2020.07776.
- [156] P. Wang, Y. Zhang, Y. Liu, J. Wang, X. Hu, J. Zheng, Z. Deng, Effects of Tube Structure on the Aerodynamic Characteristics of Evacuated Tube Transport System, *IEEE Transactions on Applied Superconductivity* 31 (2021). doi:10.1109/TASC.2021.3091059.
- [157] N. V. Queipo, R. T. Haftka, W. Shyy, T. Goel, R. Vaidyanathan, P. Kevin Tucker, Surrogate-based analysis and optimization, *Progress in Aerospace Sciences* 41 (2005) 1–28. doi:10.1016/J.PAEROSCI.2005.02.001.
- [158] S. Obayashi, T. Tsukahara, Comparison of Optimization Algorithms for Aerodynamic Shape Design, *AIAA Journal* 35 (1997) 1413–1415. doi:10.2514/2.251.
- [159] J. Muñoz-Paniagua, J. García, A. Crespo, Genetically aerodynamic optimization of the nose shape of a high-speed train entering a tunnel, *Journal of Wind Engineering and Industrial Aerodynamics* 130 (2014) 48–61. doi:10.1016/J.JWEIA.2014.03.005.
- [160] T. Rogalsky, S. Kocabiyik, R. W. Derksen, Differential evolution in aerodynamic optimization, *Canadian Aeronautics and Space Journal* 46 (2000) 183–190.
- [161] C. Gilkeson, V. Toropov, H. Thompson, M. Wilson, N. Foxley, P. Gaskell, Dealing with numerical noise in CFD-based design optimization, *Computers & Fluids* 94 (2014) 84–97. doi:10.1016/j.compfluid.2014.02.004.
- [162] V. Toropov, U. Schramm, A. Sahai, R. Jones, T. Zeguer, Design Optimization and Stochastic Analysis based on the Moving Least Squares Method, in: *6th World Congresses of Structural and Multidisciplinary Optimization*, Rio de Janeiro, 2005.
- [163] K. K. Choi, B. D. Youn, R.-J. Yang, Moving least square method for reliability-based design optimization, in: *4th World Congress of Structural and Multidisciplinary Optimization*, Dalian, China, 2001.
- [164] S. Wang, R. Wang, Y. Xia, Z. Sun, L. You, J. Zhang, Multi-objective aerodynamic optimization of high-speed train heads based on the PDE parametric modeling, *Structural and Multidisciplinary Optimization* 2021 (2021) 1–20. doi:10.1007/S00158-021-02916-0.
- [165] Y. Shuanbao, G. Dilong, S. Zhenxu, Y. Guowei, C. Dawei, Optimization design for aerodynamic elements of high speed trains, *Computers*

- & *Fluids* 95 (2014) 56–73. doi:10.1016/J.COMPFLUID.2014.02.018.
- [166] M. Suzuki, K. Nakade, Multi-Objective Design Optimization of High-Speed Train Nose, *Journal of Mechanical Systems for Transportation and Logistics* 6 (2013) 54–64. doi:10.1299/JMTL.6.54.
- [167] B. Evans, T. Morton, L. Sheridan, O. Hassan, K. Morgan, J. W. Jones, M. Chapman, R. Ayers, I. Niven, Design optimisation using computational fluid dynamics applied to a land-based supersonic vehicle, the BLOODHOUND SSC, *Structural and Multidisciplinary Optimization* 47 (2013) 301–316. doi:10.1007/S00158-012-0826-0.
- [168] J. Townsend, B. Evans, T. Tudor, Aerodynamic optimisation of the rear wheel fairing of the land speed record vehicle BLOODHOUND SSC, *The Aeronautical Journal* 120 (2016) 930–955. doi:10.1017/AER.2016.40.
- [169] M. R. Uddin, T. S. Saniat, S. Salehin, M. H. Rahman, Drag-based aerodynamic braking system for the Hyperloop: a numerical study, *Transactions of the Canadian Society for Mechanical Engineering* 45 (2021) 1–10. doi:10.1139/tcsme-2019-0120.
- [170] B. Evans, J. Townsend, O. Hassan, K. Morgan, R. Ayers, M. Chapman, A. Green, On the subsonic and low transonic aerodynamic performance of the land speed record car, Bloodhound LSR, *Proceedings of the Institution of Mechanical Engineers, Part G: Journal of Aerospace Engineering* 236 (2022) 1895–1921. doi:10.1177/09544100211046159.
- [171] R. Noble, *Thrust 2: A Memory*, Amberley Publishing, 2022.
- [172] SpaceX, SpaceX Hyperloop Test-Track Specification, 2016. URL: <https://aviation.report/whitepapers/spacex-hyperloop-test-track-specification>, accessed: 17-09-2021.
- [173] T. Dong, G. Minelli, J. Wang, X. Liang, S. Krajnović, The effect of ground clearance on the aerodynamics of a generic high-speed train, *Journal of Fluids and Structures* 95 (2020) 102990. doi:10.1016/J.JFLUIDSTRUCTS.2020.102990.
- [174] G. Doig, S. Wang, H. Kleine, J. Young, Aerodynamic Analysis of Projectiles in Ground Effect at Near-Sonic Mach Numbers, *AIAA Journal* 54 (2016) 150–160. doi:10.2514/1.J054114.
- [175] G. Doig, Transonic and supersonic ground effect aerodynamics, *Progress in Aerospace Sciences* 69 (2014) 1–28. doi:10.1016/J.PAEROSCI.2014.02.002.
- [176] T. T. G. Le, J. Kim, K. S. Jang, K. S. Lee, J. Ryu, Numerical study of unsteady compressible flow induced by multiple pods operating in the Hyperloop system, *Journal of Wind Engineering and Industrial Aerodynamics* 226 (2022). doi:10.1016/J.JWEIA.2022.105024.
- [177] M. O. Mirza, Z. Ali, Numerical analysis of aerodynamic characteristics of multi-pod hyperloop system, *Proceedings of the Institution of Mechanical Engineers, Part G: Journal of Aerospace Engineering* (2022). doi:10.1177/09544100221137483.
- [178] J. Törnell, S. Sebben, P. Elofsson, Experimental investigation of a two-truck platoon considering inter-vehicle distance, lateral offset and yaw, *Journal of Wind Engineering and Industrial Aerodynamics* 213 (2021) 104596. doi:10.1016/J.JWEIA.2021.104596.
- [179] P. Schito, F. Braghin, Numerical and Experimental Investigation on Vehicles in Platoon, *SAE International Journal of Commercial Vehicles* 5 (2012) 63–71. doi:10.4271/2012-01-0175.
- [180] W. Jia, K. Wang, A. Cheng, X. Kong, X. Cao, Q. Li, Air flow and differential pressure characteristics in the vacuum tube transportation system based on pressure recycle ducts, *Vacuum* 150 (2018) 58–68. doi:10.1016/J.VACUUM.2017.12.023.
- [181] W. Jia, K. Zhang, C. Wang, J. Yan, Z. Liu, Q. Li, Study on the influence of HRD on aerodynamic heat diffusion of VTT system under different blocking ratios, *Vacuum* 179 (2020). doi:10.1016/J.VACUUM.2020.109502.
- [182] F. Lluesma-Rodríguez, T. González, S. Hoyas, CFD Simulation of a Hyperloop Capsule Inside a Low-Pressure Environment Using an Aerodynamic Compressor as Propulsion and Drag Reduction Method, *Applied Sciences* 11 (2021). doi:10.3390/APP11093934.
- [183] J. Ahn, B. Kim, J. Kim, H. Kwon, W. Cho, Characteristics of a Flow Field Generated by a Breach on an Evacuated Tube, *International Journal of Aeronautical and Space Sciences* 23 (2022) 848–858. doi:10.1007/s42405-022-00479-y.
- [184] C. D. Donaldson, R. S. Snedeker, A study of free jet impingement. Part 1. Mean properties of free and impinging jets, *Journal of Fluid*

- Mechanics 45 (1971) 281–319. doi:10.1017/S0022112071000053.
- [185] V. Vuorinen, J. Yu, S. Tirunagari, O. Kaario, M. Larmi, C. Duwig, B. J. Boersma, Large-eddy simulation of highly underexpanded transient gas jets, *Physics of Fluids* 25 (2013) 016101. doi:10.1063/1.4772192.
- [186] J. Ackroyd, Thrust 2 – design of the world land speed record car, *Proceedings of the Institution of Mechanical Engineers, Part D: Transport Engineering* 199 (1985) 239–264. doi:10.1243/PIME_PROC_1985_199_165_01.
- [187] S. Bao, X. Hu, J. Wang, T. Ma, Y. Rao, Z. Deng, Numerical study on the influence of initial ambient temperature on the aerodynamic heating in the tube train system, *Advances in Aerodynamics* 2 (2020). doi:10.1186/S42774-020-00053-8.
- [188] P. Zhou, J. Zhang, Aerothermal mechanisms induced by the super high-speed evacuated tube maglev train, *Vacuum* 173 (2020). doi:10.1016/J.VACUUM.2019.109142.
- [189] J. Wang, S. Bao, X. Hu, H. Li, Z. Deng, Numerical Study on the Influence of the Speed on the Aerodynamic Thermal in the HTS Maglev-Evacuated Tube Transport System, *IEEE Transactions on Applied Superconductivity* 31 (2021). doi:10.1109/TASC.2021.3099776.
- [190] National Research Council, *Accelerated Aging of Materials and Structures: The Effects of Long-Term Elevated-Temperature Exposure*, The National Academies Press, Washington DC, 1999. doi:10.17226/9251.